

Drop encapsulation and bubble bursting in surfactant-laden flows in capillary channels

P. Pico ¹, L. Kahouadji ^{1,*}, S. Shin ², J. Chergui ³, D. Juric ^{3,4} and O. K. Matar ¹

¹*Department of Chemical Engineering, Imperial College London, South Kensington Campus, London SW7 2AZ, United Kingdom*

²*Department of Mechanical and System Design Engineering, Hongik University, Seoul 121-791, Republic of Korea*

³*Université Paris Saclay, Centre National de la Recherche Scientifique (CNRS), Laboratoire Interdisciplinaire des Sciences du Numérique (LISN), 91400 Orsay, France*

⁴*Department of Applied Mathematics and Theoretical Physics, University of Cambridge, Cambridge CB3 0WA, United Kingdom*



(Received 7 August 2023; accepted 23 January 2024; published 1 March 2024)

We present a parametric study of the unsteady phenomena associated with the flow of elongated gas bubbles traveling through liquid-filled square capillaries under high Weber number conditions. These conditions induce the formation of an indentation at the back of the bubble that commonly gives way to a deep reentrant liquid jet penetrating the bubble. Subsequent steps include pinch-off events in the penetrating liquid to generate one or multiple encapsulated drops which may coalesce, in conjunction with the bursting of the bubble-liquid interface by either the liquid jet or the drops. Some of these interfacial instabilities have previously been reported experimentally and numerically for liquid-liquid flow in microchannels. We carry out three-dimensional direct numerical simulations based on a hybrid interface-tracking/level-set method capable of accounting for the presence and dynamic exchange of surfactants between the liquid bulk phase and the liquid-gas interface. Our results indicate that the delicate interplay among inertia, capillarity, viscosity, surfactant adsorption/desorption kinetics, and Marangoni stresses has a dramatic influence over the nonaxisymmetric morphological structures of the encapsulated drops-elongated bubble. This strong coupling also influences the pinch-off time, penetration depth of the liquid, and number, size, and velocity of the encapsulated drops across the bubble. The observed phenomena are summarized in three main morphological regimes based on surfactant-related parameters and dimensionless groups. A discussion of the flow regime maps is also provided.

DOI: [10.1103/PhysRevFluids.9.034001](https://doi.org/10.1103/PhysRevFluids.9.034001)

I. INTRODUCTION

The problem of gas bubbles propagating in confined capillary channels has been the subject of extensive theoretical, experimental, and numerical investigation (see Etminan *et al.* [1] and references therein). In addition to being a classic problem in fluid mechanics, as seen in the

*l.kahouadji@imperial.ac.uk

Published by the American Physical Society under the terms of the [Creative Commons Attribution 4.0 International](https://creativecommons.org/licenses/by/4.0/) license. Further distribution of this work must maintain attribution to the author(s) and the published article's title, journal citation, and DOI.

now-seminal works of Bretherton [2], Taylor [3], and Schwartz *et al.* [4], these flows are central to multiple applications in technology development and are found in several real-life systems. To name a few examples, gas-liquid interfaces in the micro- and capillary scale are involved in two-phase coolers [5], CO₂ sequestration and storage microdevices [6], obstructed pulmonary airways [7], and volcanic conduits [8]. Since the early works mentioned above, extensive efforts have been undertaken to understand the phenomena dictating the bubble's behavior along with the surrounding thin liquid film, largely through an idealization of the operating conditions and the morphology of the bubble itself as a flat cylinder bounded by two semispherical menisci. It is well known through experiments [3] and theory [2] that the film thickness of the flat region scales as $h \sim Ca_b^{2/3}$ within the realms of vanishing capillary, Ca_b , and Reynolds numbers, Re_b , and as $h \sim Ca_b^{2/3}/(1 + Ca_b^{2/3})$ for $Ca_b < 2$ [9,10]. As inertial effects become non-negligible, Han and Shikazono [11] proposed a correction to the scaling exponents of Ca_b and the introduction of the Weber number, We_b , in the scaling law expression. Particular attention has also been placed on exploring the influence of Ca_b on the pressure drop ahead of the bubble [12], mapping the full bubble topological profiles [13], analyzing the undulatory structures that emerge in the vicinity of the bubble rear [14,52] as inertial effects begin to dominate, and predicting the final shape of the front meniscus [15].

Other researchers have delved into the problem by deviating from the traditional idealized assumptions of circular and straight channels, absence of surface-active materials, fully dominating capillary forces, and rigid spherical interfaces. These studies have elucidated critical differences between the steady-state and axisymmetrical features of idealized bubbles and those that adhere to more realistic scenarios. For square or rectangular channel cross sections, the experiments of Chen *et al.* [16,17] and numerical simulations of Magnini and Matar [18] and Magnini *et al.* [19] have uncovered significant angular and axial nonuniformities in the liquid film thickness, whereby the effects of the rigid walls tend to flatten the interface at the channel's center-line ($h_{\min} \sim Ca_b$), depleting it of the liquid phase, and inducing the formation of large lobes protruding towards the channel corners in the cross section ($h \sim Ca_b^{0.445}$). Furthermore, noncircular channels promote an exponential thinning of the liquid film along the bubble length from the nose to the rear section, as reported in Lister *et al.* [20], Magnini and Matar [18]. The effects of other nonideal geometries have been examined by Sauzade and Cubaud [21], who carried out an experimental campaign to study the distortion of a train of bubbles in a constricting-expanding microchannel under varying Ca_b and bubble packing conditions. This study provided evidence for the occurrence of bubble width-to-length ratio hysteresis across the sinusoidal structures of the channel and the attenuation of these effects with decreasing Ca_b .

A wide array of investigations have focused on illustrating the effects of (in)soluble surfactants on liquid-gas confined flows, placing particular emphasis on their influence on liquid film thickness, bubble deformation, and pressure drop (see Olgac and Muradoglu [22] and references). The literature largely agrees that, under typical surfactant characteristics and negligible inertia, the liquid film displays a thickening response to surfactants of the order of 1 to $4^{2/3}$ times that predicted by the expression of Bretherton [2] for uncontaminated interfaces. This thickening has been reported to vary with Ca_b , surface elasticity, and across the bubble length due to Marangoni-related mechanisms, which act in opposition to liquid drag forces as they push the surfactants towards the bubble back. Nonetheless, the numerical results of Ghadiali and Gaver [23] in the context of pulmonary airways suggest the possibility of liquid film thinning surfactant actions under conditions of large bulk Péclet number, $Pe_c \gg 1$, and $Ca_b > 10^{-1}$ due to a bifurcation and enhancement of Marangoni stresses, which drive fluid away from the thin film region and towards the bubble nose. In terms of pressure drop and bubble velocity, it has been shown that surfactants tend to increase the pressure drop across the dispersed phase [24,25] and significantly reduce the bubble's mobility along its length [26]. Batchvarov *et al.* [27] carried out a comprehensive computational exploration of multiple surfactant characteristics and dimensionless groups with the novelty of introducing inertial effects ($Re = 443\text{--}728$) to the analysis. A key finding of this work is the surfactant-induced dampening of the bubble's rear interfacial oscillatory structures,

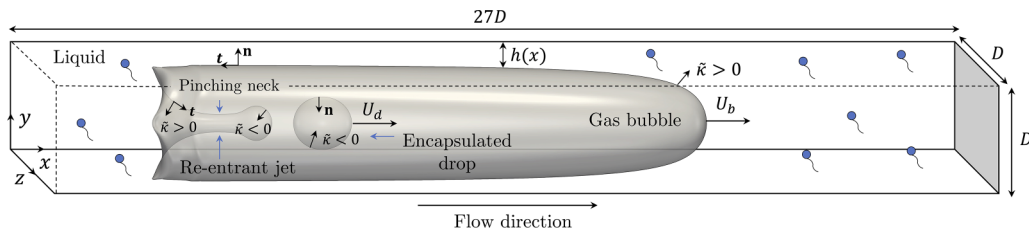


FIG. 1. (Not to scale) Schematic of simulation setup, reentrant liquid jet penetrating the bubble, and encapsulated drop. The direction of outwards pointing normal vectors, liquid film thickness, $h(x)$, and curvature sign according to the adopted convention are also highlighted. The location of the Cartesian axis represents the outset of the geometrical domain ($x = 0, y = 0, z = 0$).

typical of systems with non-negligible inertia, together with the evidence provided to affirm that this process is entirely Marangoni-driven rather than a consequence of localized lowered surface tension. Moreover, this investigation addressed the effect of low solubility surfactants, detecting a clear arrangement of the bubble's morphology into two separate regions: one fully covered in surfactants and of reduced mobility, extending from the bubble rear to a portion in the streamwise direction that depends on Pe_c , and one of diminished surfactant concentration that stretches to the bubble nose, behaving similarly to clean interfaces.

A noteworthy sequence of events transpires in the bubble as Ca_b is increased to a critical value that strongly depends on its length and Re . As reported in a number of investigations [15,28–30], the combination of reduced dominance of capillary forces (given by larger Ca) and heightened inertia (given by larger Re , leading to larger $We = Ca Re$) has a distorting impact on the curvature of the front and back menisci, dragging both interfaces towards the main flow direction and causing the bubble to adopt an elongated, “bullet-like” shape. With the continued increase in inertial and viscous forces, the bubble's rear undergoes a curvature inversion, enabling the liquid phase to infiltrate the bubble's domain and form a small liquid jet. The threshold conditions that induce this curvature inversion phenomenon have been reported to be $We \approx 20$ for $Re \sim O(10^1)$ in circular channels by Giavedoni and Saita [15] and $Ca \gtrsim 1$ for $Re \rightarrow 0$ in circular/square channels by Refs. [10,29,30]. As briefly shown in Sec. III A, our surfactant-free simulations allow us to place the threshold within the range $17 < We < 20$ for $Re \sim O(10^2)$ in square capillaries.

The fate of the liquid infiltrating the bubble is highly influenced by a complex interplay of phenomena that might culminate in a continuous growth in the main axial or radial direction, or in its capillary breakup to encapsulate and entrap liquid drops within the bubble (see Fig. 1). This liquid infiltration process shares qualitative similarities with other systems relevant to engineering applications, such as sheet cavitation. In this type of cavitation, the adverse pressure gradient induces the development and spreading of a reentrant liquid jet in the upstream direction underneath the cavity sheet, separating it from the solid surface [31].

The type of encapsulation described above has been observed experimentally in the works of Goldsmith and Mason [32] and Olbricht and Kung [33] in liquid-liquid flows. Similar findings are reported in a limited number of numerical pursuits on multiphase confined flows, including the investigations of Tsai and Miksis [34] and Izbassarov and Muradoglu [35] for contracting/expanding capillaries in Newtonian and viscoelastic fluids, respectively, Pozrikidis [36] for buoyancy-driven flows of viscous drops, Nath *et al.* [37] for liquid drops in creeping flow, and Andreadaki *et al.* [38] and Atasi *et al.* [39] for gas bubbles in the absence/presence of surfactants, respectively. The last three studies have provided an examination of the specific conditions that induce the encapsulation phenomenon, a general elucidation of the mechanisms at play, and an overview of the encapsulation aftermath. Nath *et al.* [37] have remarked that, in the inertialess limit and considering fully circular channels, there exists a critical Ca_b beyond which drop breakup and entrapment events will occur. The authors found this critical value to decrease (increase) with the initial drop-to-channel radius

(dispersed-to-continuous phase viscosity). Andredaki *et al.* [38] and Atasi *et al.* [39] have recently laid the groundwork for the formulation of general encapsulation and breakup regime maps for $Re \ll 1$, bounded by We_B and the relationship between inertia and pressure drop across the channel in the former, and Ca_b and the relative importance of interface surfactant adsorption/desorption in the latter case.

Despite these initial efforts, much remains unknown and unexplored about these encapsulation events. Notably, a quantitative and phenomenological description of the underlying dynamics that govern each step of the process is needed, in combination with a thorough inspection of the reentrant liquid jet characteristics. It is also crucial to address the multiple examples of interfacial singularities inherent to the system at hand, which have yet to be analyzed from the perspective of the well-established problem of capillary breakup, from which multiple parallels naturally emerge between our system and others (e.g., contracting liquid ligaments and inkjet printing). Likewise, an analysis of the evolution of the drops beyond pinch-off is required as it is a topic much less understood than the steps that precede it [40] and could be crucial to potential applications [35]. Finally, and as will be seen in this paper, extending the set of surfactant parameters explored from those of Atasi *et al.* [39] uncovers new encapsulation and breakup outcomes, which allows us to expand and enhance the original regime maps. The main objective of this paper is therefore to carry out an extensive characterization of the reentrant liquid jet formation and (post) pinch-off dynamics, taking into account the interaction between surfactants and inertia, capillarity, and viscosity in a noncircular channel geometry, which correspond to nonidealities of interest, as seen in the foregoing literature review.

The rest of the paper is organized as follows: Sec. II introduces our problem formulation, computational setup, and numerical approach. A discussion of our results is presented in Sec. III, where we focus first on encapsulation in clean interfaces followed by an examination of surfactant-laden systems. Finally, concluding remarks are provided in Sec. IV.

II. NUMERICAL METHODS AND PROBLEM FORMULATION

A. Numerical modeling and nondimensionalization

We consider a horizontal liquid-filled square capillary of width and height D in a Cartesian three-dimensional domain, $\mathbf{x} = (x, y, z)$, with an elongated gas bubble propagating through its interior (see Fig. 1). Assuming incompressible flow, Newtonian fluids, and negligible gravitational effects, we perform direct numerical simulations (DNS) based on the two-phase Navier-Stokes equations and a hybrid front-tracking/level-set method to handle the interface and surface tension forces. This method, as formulated and implemented in Shin and Juric [41], is coupled with the resolution of surfactant transport and exchange between the interface and the liquid phase bulk, as described in Shin *et al.* [42]. The relevant variables involved in the system have been rendered dimensionless (denoted by tildes) by using the scalings depicted in Eq. (1),

$$\begin{aligned} \tilde{\mathbf{x}} &= \frac{\mathbf{x}}{D}, & \tilde{\mathbf{u}} &= \frac{\mathbf{u}}{U_a}, & \tilde{t} &= \frac{t}{D/U_a}, & \tilde{p} &= \frac{p}{\rho_l U_a^2}, & \tilde{\sigma} &= \frac{\sigma}{\sigma_s}, \\ \tilde{\Gamma} &= \frac{\Gamma}{\Gamma_\infty}, & \tilde{C} &= \frac{C}{C_\infty}, & \tilde{C}_s &= \frac{C_s}{C_\infty}, \end{aligned} \quad (1)$$

where \mathbf{u} , t , p , σ , Γ , C , and C_s represent velocity, time, pressure, surface tension, interfacial surfactant concentration, bulk surfactant concentration, and bulk surfactant concentration in the vicinity of the interface, respectively. The physical parameters included in the scaling correspond to the width of the channel, D , the average inlet velocity of the liquid, U_a , the density of the liquid phase, ρ_l , the surface tension in a surfactant-free interface, σ_s , the saturation interfacial concentration, Γ_∞ , and the initial bulk surfactant concentration, C_∞ , in line with the scaling proposed by Batchvarov *et al.* [27] for a similar system. In what follows, we refer to each variable by its name to refer to its

dimensionless version, unless stated otherwise, and add the subscript b to signify that the variable is reported at the bubble nose.

The mass and momentum equations are written in dimensionless form and according to a ‘‘one-fluid’’ formulation:

$$\begin{aligned} \nabla \cdot \tilde{\mathbf{u}} &= 0, \\ \tilde{\rho} \left(\frac{\partial \tilde{\mathbf{u}}}{\partial \tilde{t}} + \tilde{\mathbf{u}} \cdot \nabla \tilde{\mathbf{u}} \right) &= -\nabla \tilde{p} + \frac{1}{\text{Re}} \nabla \cdot [\tilde{\mu}(\nabla \tilde{\mathbf{u}} + \nabla \tilde{\mathbf{u}}^T)] + \frac{1}{\text{Re Ca}} \int_{\tilde{A}(\tilde{t})} (\tilde{\sigma} \tilde{\kappa} \mathbf{n} + \nabla_s \tilde{\sigma}) \delta(\tilde{\mathbf{x}} - \tilde{\mathbf{x}}_f) d\tilde{A}, \end{aligned} \quad (2)$$

$$\tilde{\rho}(\mathbf{x}, t) = \rho_g + (\rho_l - \rho_g) \mathcal{J}(\mathbf{x}, t), \quad \tilde{\mu}(\mathbf{x}, t) = \mu_g + (\mu_l - \mu_g) \mathcal{J}(\mathbf{x}, t), \quad (3)$$

where $\mathcal{J}(\mathbf{x}, t)$ is a smoothed Heaviside function that adopts the value of zero in the gas phase and unity in the liquid phase, ρ the density, and μ the viscosity of the fluids. Here we denote the liquid and gas phases with the subscripts l and g , respectively. The normal and tangential components of the surface tension forces are represented by the last two terms on the right-hand side (r.h.s.) of Eq. (2), wherein $\tilde{\kappa}$ corresponds to twice the mean interface curvature, \mathbf{n} to a unit normal to the interface, $\delta(\tilde{\mathbf{x}} - \tilde{\mathbf{x}}_f)$ to a Dirac delta function that is zero everywhere except for the interface (located at $\tilde{\mathbf{x}} = \tilde{\mathbf{x}}_f$), $\tilde{A}(\tilde{t})$ to the time-dependent interface area, and ∇_s to the surface gradient operator [43,44]. We adopt the convention that positive \mathbf{n} vectors point outwards from the interface towards the liquid phase. Accordingly, positive values of $\tilde{\kappa}$ describe a convex interface, as exemplified in Fig. 1. As is typical in front tracking, the Lagrangian interface is advected by integrating $d\mathbf{x}_f/dt = \mathbf{V}_f$, where the vertices of the Lagrangian triangular mesh discretizing the interface, \mathbf{x}_f , are displaced in time by the fluid velocity, \mathbf{V}_f , at those vertices.

Note that the gas phase dynamics are not neglected within this one-fluid formulation and are resolved along with that of the liquid via solution of Eqs. (2) and (3) with the density and viscosity defined by Eqs. (3). Consequently, the tangential component of the interfacial stress is finite with further contributions to it arising from the surface tension gradients; the latter owe their existence to the interfacial surfactant concentration gradients, as will be discussed below.

The mass conservation equations of surfactant species at the interface and bulk are given by Eqs. (4) and (5) and the source term representing surfactant exchange between the interface and the bulk region immediately adjacent is given by Eq. (6):

$$\frac{\partial \tilde{\Gamma}}{\partial \tilde{t}} + \nabla_s \cdot (\tilde{\Gamma} \tilde{\mathbf{u}}_t) = \frac{1}{\text{Pe}_s} \nabla_s^2 \tilde{\Gamma} + \text{Bi}(k\tilde{C}_s(1 - \tilde{\Gamma}) - \tilde{\Gamma}), \quad (4)$$

$$\frac{\partial \tilde{C}}{\partial \tilde{t}} + \tilde{\mathbf{u}} \cdot \nabla \tilde{C} = \frac{1}{\text{Pe}_c} \nabla \cdot (\nabla \tilde{C}), \quad (5)$$

$$\mathbf{n} \cdot \nabla \tilde{C}|_{\text{interface}} = -\text{Pe}_c \text{Da} [k\tilde{C}_s(1 - \tilde{\Gamma}) - \tilde{\Gamma}], \quad (6)$$

where $\tilde{\mathbf{u}}_t = (\tilde{\mathbf{u}} \cdot \mathbf{t})\mathbf{t}$ is the projection of the interface velocity vector, $\tilde{\mathbf{u}}_s$, on the interface unit tangent, \mathbf{t} . The dependence of surface tension on local interface surfactant concentration is represented by a nonlinear equation of state derived from Langmuir adsorption isotherm, as expressed in Eq. (7),

$$\tilde{\sigma} = \max(\epsilon_\sigma, 1 + \beta_s \ln(1 - \tilde{\Gamma})), \quad (7)$$

where $\beta_s = \mathcal{R}T\Gamma_\infty/\sigma_s$ is the surfactant elasticity number; \mathcal{R} and T are the thermodynamic ideal gas constant and temperature, respectively. The nonlinear equation of state described above is valid for very dilute systems in which $\Gamma \ll \Gamma_\infty$. As Γ increases, the equation of state yields unphysical negative values of surface tension. To circumvent this, a limiting value for $\tilde{\sigma}$, $\epsilon_\sigma = 0.05$, has been introduced, in accordance with Muradoglu and Tryggvason [45] and Shin *et al.* [42]. The tangential surface stresses or Marangoni stresses, extensively discussed throughout the paper, are calculated as $\tilde{\tau}_m \equiv \nabla_s \tilde{\sigma} \cdot \mathbf{t} = -\beta_s \frac{1}{1-\tilde{\Gamma}} \nabla_s \tilde{\Gamma} \cdot \mathbf{t}$ [see last term of Eq. (2)]. The dimensionless groups that appear

in the above equations and that characterize the system are defined as follows:

$$\begin{aligned} \text{Re} &= \frac{\rho_l U_a D}{\mu_l}, & \text{Ca} &= \frac{\mu_l U_a}{\sigma_s}, & \text{Pe}_c &= \frac{U_a D}{D_c}, & \text{Pe}_s &= \frac{U_a D}{D_s}, \\ \text{Bi} &= \frac{k_d D}{U_a}, & \text{Da} &= \frac{\Gamma_\infty}{DC_\infty}, & k &= \frac{k_a C_\infty}{k_d}, \end{aligned} \quad (8)$$

where Re and Ca are the Reynolds and capillary numbers, respectively ($\text{We} = \text{Ca Re}$, and $\text{Oh} = \sqrt{\text{Ca}/\text{Re}}$). Pe_c and Pe_s are the bulk and interfacial Péclet numbers, which provide a measure of the importance of inertia relative to surfactant mass diffusion across the interface (modulated by a diffusivity D_c) or the bulk (modulated by a diffusivity D_s), respectively; Bi represents the Biot number, describing the competition between convective, $t_{\text{conv}} = D/U_a$, and interface surfactant desorption, $t_{\text{des}} = k_d^{-1}$, timescales. The Damköhler number, Da, provides a dimensionless measure of the initial interface saturation, and the number k reflects the interplay between the characteristic timescales of interface surfactant adsorption, $t_{\text{ad}} = (k_a C_\infty)^{-1}$, and desorption. We note that gravitational effects have not been taken into account in this study. Hence, we run our simulations with vanishing Bond number, $\text{Bo} \equiv (\rho_l - \rho_g)gD^2/\sigma_s = 0$.

For an exhaustive description of the discretization schemes and numerical framework employed for solving the above mentioned governing equations, we refer the reader to Shin *et al.* [42,44] and to Shin and Juric [43] for a comprehensive account of the hybrid front-tracking/level-set method, also called Level Contour Reconstruction Method (LCRM). Here we present a short summary of the most relevant aspects. The LCRM considers the combination of a fixed structured Eulerian grid for the resolution of field equations and a moving and deforming Lagrangian grid for the interface, discretized via an unstructured triangular mesh. These interface elements are consequently advected through the integration of the Lagrangian equation $d\mathbf{x}_f/dt = \mathbf{v}$, where \mathbf{v} corresponds to the interface velocity, which is interpolated from the Eulerian grid. This integration is carried out with a second-order Runge-Kutta method. The spatial derivatives of the fields in the Eulerian grid are discretized through a standard cell-centered scheme for all terms, with the exception of the nonlinear convective terms, for which a second-order essentially nonoscillatory (ENO) procedure is used [46,47]. For the viscous term in the momentum equation, a second-order centered difference scheme is employed. A second-order Gear method [48] is adopted for the temporal terms, with an implicit time integration for the viscous terms. The time step is set to be adaptive, according to the following criterion: $\Delta t = \min\{\Delta t_{\text{cap}} = \frac{1}{2}\sqrt{\frac{(\rho_l + \rho_g)\Delta x^3}{\pi\sigma_s}}, \Delta t_{\text{vis}} = \frac{\rho_g \Delta x^2}{6\mu_l}, \Delta t_{\text{CFL}} = \frac{\Delta x}{|u_{\text{max}}|}, \Delta t_{\text{int}} = \frac{\Delta x}{|V_{\text{int}}|}\}$, where the time steps relate to viscosity, capillarity, Courant-Friedrichs-Lewy condition, and interface, respectively; Δx is the minimum cell size, u_{max} is the maximum fluid velocity, and V_{int} is the maximum interface velocity. The time step related to the interface was found to be the limiting time step in all of our simulations [$\Delta t_{\text{int}} \sim O(10^{-7})$ s].

B. Simulation setup

As depicted in Fig. 1, our simulation domain consists of a three-dimensional rectangular box of dimensions $27D \times D \times D$, corresponding to the x (channel length), y (channel height), and z (channel width) directions, respectively. The value of the channel length was selected to ensure the attainment of a steady-state bubble propagation for $\text{We} < 10$, following the results of Batchvarov *et al.* [27] and Magnini and Matar [18]. Under conditions of $\text{We} > 10$, highly unsteady encapsulation/bursting phenomena are detected in the system. The channel length chosen allowed for the observation of all relevant phenomena, including the formation of the reentrant jet, drop encapsulations and coalescence events, and bubble bursting, for all conditions tested. The elongated bubble was initialized in quiescent conditions close to the channel inlet and at the center line of the y and z directions as a horizontal cylinder of length $3.12D$ with two hemispherical caps of diameter $0.94D$ on each end. A fully developed liquid velocity profile was imposed at the channel inlet with

a Neumann condition for pressure ($\partial p / \partial \mathbf{n} = 0$). All walls were treated as no-slip boundaries, and Neumann conditions were imposed for all variables at the outlet. The bubble-liquid interface was initially covered with surfactant of uniform concentration Γ_0 , determined from an initial equilibrium between surfactant adsorption and desorption [last term on the r.h.s. of Eq. (4) equal to zero], which, assuming $C_s = C_\infty$ initially, reads

$$\Gamma_0 = \frac{k}{k+1} \Gamma_\infty. \quad (9)$$

This setup closely resembles the approaches followed in previous numerical investigations for similar systems [25,37,39].

We explore the effect of the dimensionless numbers and flow parameters that characterize the system [see Eq. (8)] considering the following ranges: $Ca = 0.0089\text{--}0.0693$ ($We = 3.94\text{--}30.70$, $Oh = 4.48 \times 10^{-3}$ to 1.25×10^{-2}), $Pe_{c,s} = 100$, $Bi = 0.10\text{--}1$, $Da = 0.01\text{--}1$, $k = 0.10\text{--}10.00$, and $\beta_s = 0.25\text{--}1$. For all cases simulated, the viscosity and density ratio between the phases is kept constant and in line with representative values for water and air: $\rho_l / \rho_g = 1000$ and $\mu_l / \mu_g = 100$. We define a ‘‘base’’ case from which our parametric sweep was carried out with the following conditions: $Re = 443$, $Ca = 0.0693$, $Pe_{c,s} = 100$, $Bi = 0.10$, $Da = 1$, $k = 0.10$, and $\beta_s = 0.50$. Unless stated otherwise, all results correspond to simulations under these conditions. The selection of the testing ranges was based on common values encountered in bubbly flow systems in the presence of surfactants, as reported in Atasi *et al.* [39], as well as values of We that would allow a significant disruption of the bubble back to generate the aforementioned penetrating liquid and consequent drop encapsulation [15,38]. We refer the reader to Appendix A for typical values of surfactant properties, which support our choice of dimensionless ranges, and for a description of the competing timescales in our system.

Following numerous studies making use of the numerical methods described above for inertial and capillary phenomena (see Refs. [27,49,50]), we employ a fully structured and uniform Cartesian grid divided into $54 \times 4 \times 4$ subdomains, further divided into $64 \times 32 \times 32$ cells per sub-domain, rendering a global resolution equal to $3456 \times 128 \times 128$ cells. On account of ensuring this resolution produces mesh-independent results, we have performed a mesh analysis in surfactant-free and surfactant-laden conditions, detailed in Appendix B along with other resolution considerations. In this analysis, we showcase how the chosen grid resolution guarantees mesh-independent outcomes for both global variables like kinetic energy, interfacial area, and bubble velocity, and local variables associated with interfacial singularities. These encompass the curvature inversion time, the time until the first pinch-off event of the reentrant jet, and the size of the encapsulated drops, all of which show less than 3.5% difference between mesh resolutions. Furthermore, we illustrate that our resolution is adept at accurately representing the thin liquid film encasing the bubble, as outlined in Ref. [18].

The numerical framework and simulation setup presented herein have previously been carefully validated in the context of elongated bubbles in circular capillary channels. For this validation, we refer to the work of Batchvarov *et al.* [27], in which the code was benchmarked against the well-known correlation of Han and Shikazono [11] for steady-state liquid film thickness in conditions of non-negligible inertia. For $Ca \sim O(10^{-2})$ and $Re \sim O(10^2)$, deviations of up to 10% were reported, which are within the uncertainty of the correlation. A complementary validation is reported in Appendix C to demonstrate our faithful capturing of the bubble’s main morphological regimes in square capillary channels, as proposed by Magnini and Matar [18].

To attach a physically relevant meaning to the dimensionless times quoted throughout the manuscript, we henceforth report all times starting from $\tilde{t} = 0.0$, which corresponds to the instance of the bubble rear’s curvature inversion (mentioned in Sec. I and detailed in Fig. 3 below) for each set of conditions. For the surfactant-free and low Ca cases that do not exhibit a curvature inversion (see Fig. 2), $\tilde{t} = 0.0$ was taken as the inversion time of the surfactant-free case that did undergo such process (see Sec. III A).

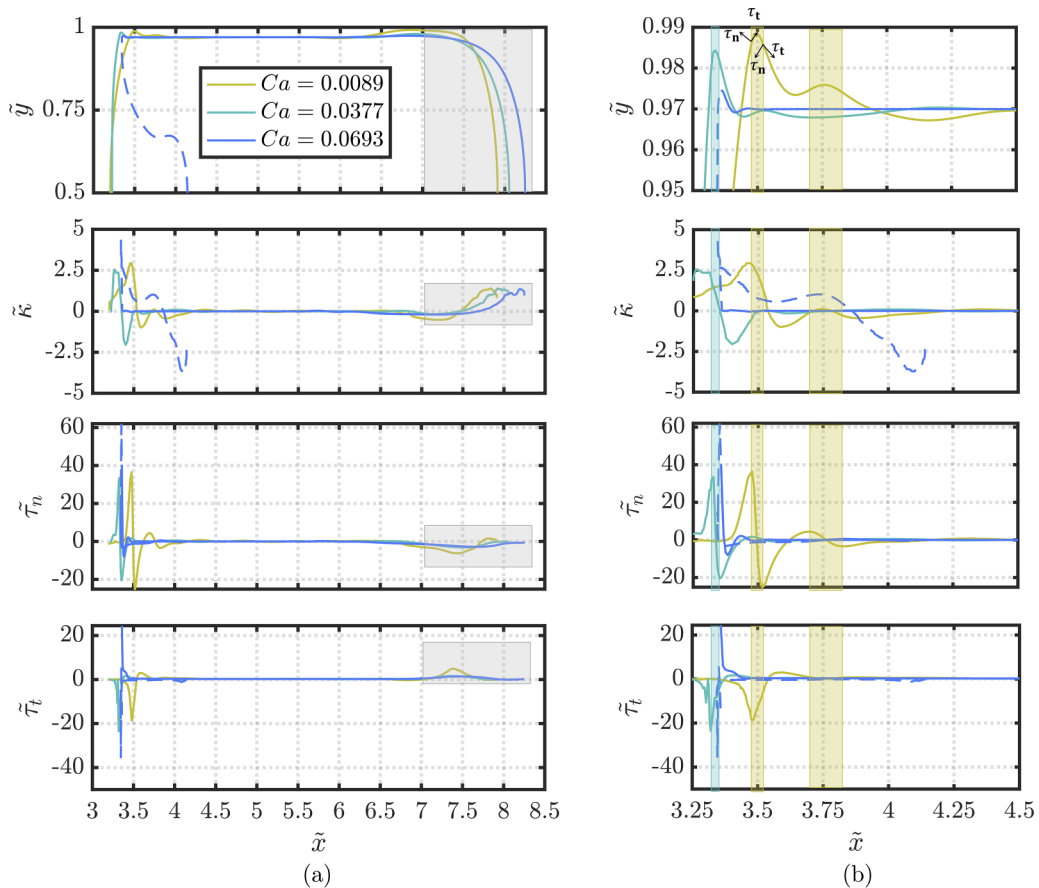


FIG. 2. Effect of Ca on bubble characteristics for surfactant-free cases at $\tilde{t} = 0.76$. (a) Full bubble length in the axial direction. (b) Zoom over the trailing undulatory structures at low Ca ($3.25 < \tilde{x} < 4.5$). From top to bottom the plots correspond to bubble-liquid interface shape, normalized mean curvature, $\tilde{\kappa}$, normalized normal component of viscous stress on the interface, $\tilde{\tau}_n$, and normalized tangential component of viscous stress on the interface, $\tilde{\tau}_t$, respectively. Dotted line for $Ca = 0.0693$ highlights the reentrant liquid jet. All other parameters remain unchanged from those specified in Sec. II B for the base case. The highlighted zones in (b) represent the areas bounded by $\tilde{\tau}_n$ local maxima and minima their projections in the \tilde{y} , $\tilde{\kappa}$, and $\tilde{\tau}_t$ profiles.

III. RESULTS AND DISCUSSION

The results of our investigation are presented in three parts. The first, Sec. III A, introduces the phenomenon of drop encapsulation by contrasting the behavior of three surfactant-free cases of varying Ca and exposed to non-negligible inertial effects ($Re = 443$, Fig. 2). The second part of the results, Sec. III B, analyzes selected cases from our surfactant-related parameter sweep (β_s , Bi , k , and Da) and quantifies their influence on drop encapsulation. The final set of results, Sec. III C, summarizes all encapsulation behaviors observed in two regime maps in the β_s - k and Bi - k spaces (see Fig. 11 below).

A. Bubble dynamics in surfactant-free cases: Tail undulations, curvature disruptions, and encapsulations

We start our discussion by showcasing the bubble topology at a two-dimensional projection in the (x, y) plane at the channel center -line ($\tilde{z} = 0.5$), as well as the normalized mean curvature,

$\tilde{\kappa}$, and the normal, $\tilde{\tau}_n$, and tangential, $\tilde{\tau}_t$, components of the viscous stress along the interface [see Figs. 2(a) and 2(b)]. Here these quantities are defined as $\tilde{\kappa} = \kappa/\kappa_c$, $\tilde{\tau}_n = \tau_n/(D/U_a)$, and $\tilde{\tau}_t = \tau_t/(D/U_a)$, respectively, where $\tau_n = (\mathbf{D} \cdot \mathbf{n}) \cdot \mathbf{n}$, $\tau_t = (\mathbf{D} \cdot \mathbf{n}) \cdot \mathbf{t}$, $\mathbf{D} = (\nabla \mathbf{u} + \nabla \mathbf{u}^T)/2$ (rate of deformation tensor), and κ_c corresponds to the curvature of a sphere with a volume equal to the initial bubble volume. Under the sign conventions adopted, $\tilde{\tau}_n > 0$ denotes stresses exerted on the interface towards the liquid phase. Conforming to previous observations [15,28–30], our plots reveal a loss of sphericity (typical of fully dominant capillary forces) at the bubble front and back with increasing Ca, in conjunction with an overall axial bubble elongation. The interface at the bubble front sharpens and expands, while the bubble back becomes progressively flattened with Ca, adopting a “bullet-like” shape ($\tilde{\kappa}_{\text{front}} > \tilde{\kappa}_{\text{back}}$). This process continues until a curvature inversion emerging from $\tilde{y} = 0.5$ is detected for Ca = 0.0693, which eventually leads to a drop encapsulation. As mentioned in Sec. 1, this type of curvature sign inversion is triggered by a combination of large Ca and Re. From the surfactant-free results shown in Fig. 2(a) at Re = 443, as well as those reported in Appendix C, which encompass various Ca and Re values (We = 2.5–50), we place the threshold value for curvature inversion in the range $17 < \text{We} < 20$. This range is fully consistent with that previously found in Giavedoni and Saita [15] [We \approx 20 for Re $\sim O(10^1)$] in circular channels.

We note that the bubble shapes presented in Fig. 2(a) correspond to the systems’ initial stages of development in terms of the reentrant jet and the front/rear menisci ($\tilde{t} = 0.76$). During these early stages, the systems are still distant from equilibrium, which is typically achieved at $\tilde{t} \approx 6$ for the nonencapsulated cases Ca = 0.0089, 0.0377 (and notably not attained for the encapsulated case, as demonstrated in both our present study and prior research; see Sec. 1). Consequently, the well-established direct relationship between liquid film thickness, $h(x)$, and Ca [2,11,18] has not materialized fully in the systems at this early stage, explaining the apparent absence of differences in $h(x)$ for varying Ca. A further discussion of the effects of Ca on $h(x)$ is provided in Appendix C, where the cross-sectional bubble shapes of the systems depicted in Fig. 2(a) are displayed and analyzed at a later time (see Fig. 13 below).

Detailing the behavior of $\tilde{\kappa}$ for Ca = 0.0693 along the interface path going from the reentrant liquid jet vertex to the bubble nose, a zone of negative curvature is first observed at $3.8 \lesssim \tilde{x} \lesssim 4.1$, followed by a positive curvature meniscus at $3.3 \lesssim \tilde{x} \lesssim 3.8$. This particular curvature sign inversion is a manifestation of the early stages that precede pinch-off and drop encapsulation. This process and its connection to other well-known systems that exhibit capillary instabilities are examined further along in this paper. Exiting the interior of the liquid jet towards the region adjacent to the liquid film ($3.3 \lesssim \tilde{x} \lesssim 7.0$), a nonuniform low curvature zone that encompasses the majority of the bubble is identified, later culminating in the high-curvature bubble nose seen for $\tilde{x} > 7.0$. Contrasting this evolution to that of the two lowest Ca, it can be noticed that the spatial location that marks the beginning of the bubble nose [sudden curvature rise from the thin-liquid film region, highlighted in gray in Fig. 2(a)] shifts to lower \tilde{x} for decreasing Ca. Notable curvature inversions at the bubble tail are also identified for the low Ca cases, expressed in the undulatory structures emphasized in Fig. 2(b). These interfacial waves, previously reported in Refs. [15,51,52], moderately diminish in frequency and amplitude with Ca at the same Re, as illustrated in the figure.

The dynamics of the bubble-liquid interface and its curvature gradients are readily mapped onto the $\tilde{\tau}_{n,t}$ spatial profiles of Fig. 2. Pertaining to the trailing undulatory structures (highlighted in yellow and green for Ca = 0.0089 and Ca = 0.0377, respectively), it is found that these are first characterized by a sudden surge in $\tilde{\tau}_n$ that terminates in a local maximum, which pushes the interface towards the channel walls and thus creates the crests of the interfacial waves. These peaks are promptly followed by a rapid $\tilde{\tau}_n$ decrease approaching a local minimum that contributes to the formation of the wave troughs by pulling the interface back towards the bubble. Concurrently, the tangential stresses feature similar inverse patterns of local maxima/minima that promote the sharpening of the crests/troughs. A substantial drop in $\tilde{\tau}_{n,t}$, mirrored by $\tilde{\kappa}$, is observed by departing from the rear undulatory region to the high-pressure central section of the bubble. $\tilde{\tau}_{n,t}$ remain quasi-constant and close to zero throughout this section until the reappearance of local maxima/minima marks the onset of the bubble nose. Note the generally higher $|\tilde{\tau}_t|$ exerted on the bubble nose at

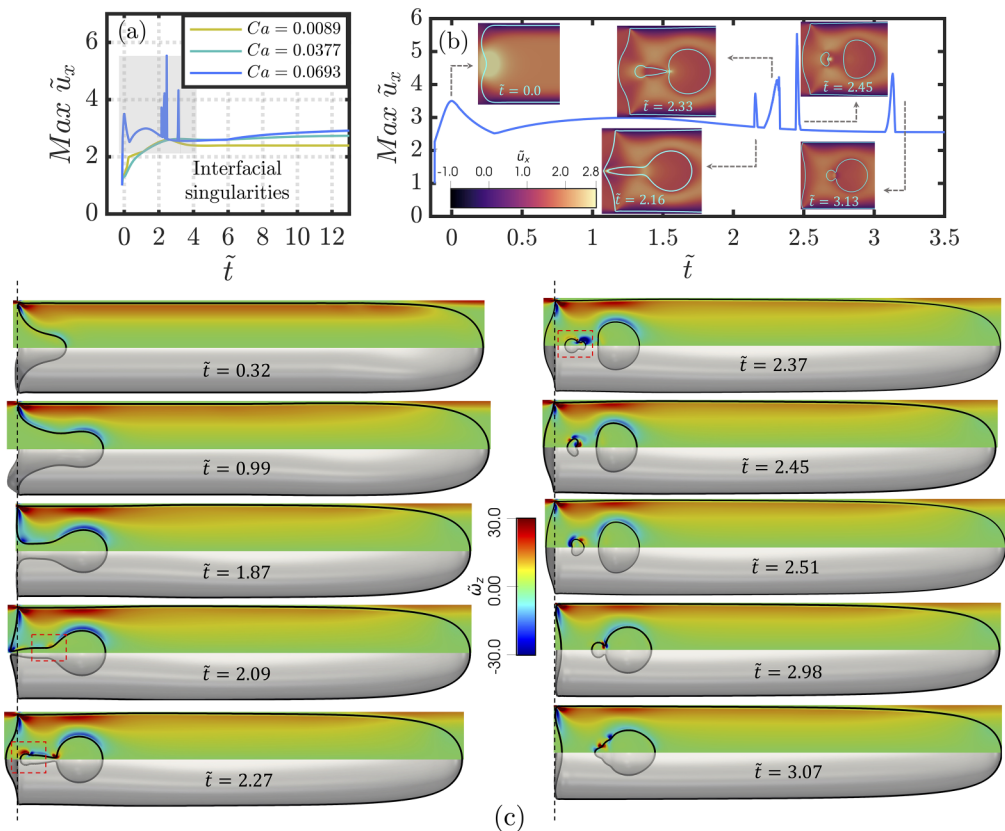


FIG. 3. Temporal evolution of interface characteristics in surfactant-free cases. (a) Maximum dimensionless velocity in the x direction. (b) Zoom on interfacial singularities found for $Ca = 0.0693$. (c) Detailed evolution of encapsulation process for $Ca = 0.0693$. Contour plots of normalized azimuthal vorticity, $\tilde{\omega}_z = \omega_z/(D/U_a)$ (top) and three-dimensional bubble shape (bottom). The interfaces of these contour plots have been translated in the x direction to have a common point of reference (marked by the black dotted line).

$\tilde{y} = 0.5$ for decreasing Ca , partly contributing to a lower curvature (more spherical) bubble front. Similar remarks about the close relationship between curvature, capillarity, and interfacial stresses have been made by Atasi *et al.* [39].

We now proceed to detail the encapsulation process by first illustrating the numerous flow singularities produced by high Ca conditions in uncontaminated interfaces. In Fig. 3(a) we plot the temporal evolution of the maximum normalized velocity in the x direction, $\text{Max } \tilde{u}_x$. This evolution reveals five major local peaks in $Ca = 0.0693$ in the interval $0 < \tilde{t} < 3.5$, which materialize in (i) the previously analyzed curvature inversion at the bubble back, (ii) and (iii) two pinch-offs that give rise to a “satellite” and a primary drop, (iv) an abrupt retraction and subsequent expansion of the former, and (v) a coalescence event between the two drops [see Fig. 3(b)]. A first description of the mechanisms by which these interfacial singularities come about is shown in Fig. 3(c), where a liquid infiltration deepening in the positive x direction takes place at $0.32 < \tilde{t} < 0.99$. The fate of this liquid structure can be understood through the hybrid lens of the well-known problems of liquid filament breakup surrounded by a gas phase [53,54] and liquid dripping faucets [55]. Our liquid jet at $\tilde{t} < 0.99$ can be thought of as a quasicylindrical liquid filament ($Oh = 0.0125$) with a low ratio between its length, $2L_{\text{jet}}$, and radius, R_{jet} undergoing end pinching.

At around $\tilde{t} = 0.99$ in Fig. 3(c), we observe a halt in jet axial growth as capillary pressure builds at the bubble rear, inducing a vertical expansion towards the channel center line ($\tilde{y} = 0.5$), creating

an essentially flat bubble back at $\tilde{t} = 1.87$ and a nascent pinching neck characterized by a high $|\tilde{\omega}_z|$ ring. The interface areas covered by the ring are further pulled in the counterflow direction, prompting an additional curvature inversion at the bubble rear and the first pinch-off thereupon (see $\tilde{t} = 2.09$). This capillary singularity promotes a swift and opposite-direction recoil of the bubble back and the newly entrapped liquid structure, thus forming the globoid-shaped bubble rear observed in $\tilde{t} = 2.27$ – 2.51 . The rapidly forming rear pinching neck witnesses the incipience of an additional capillary neck at the interior of the bubble (see highlight and high $\tilde{\omega}_z$ ring in $\tilde{t} > 2.09$). This concludes in a second pinch-off and a precipitous recoil into a satellite drop (see $\tilde{t} = 2.37$). Henceforth, we will refer to the first of these pinch-off events as “back pinch-off,” and to the second as “interior pinch-off”; the times for these events are denoted as $\tilde{t}_{p-o,bk}$ and $\tilde{t}_{p-o,int}$, respectively. These phenomena of successive back and interior pinch-offs in surfactant-free cases are in agreement with previous numerical observations [38].

The post-second pinch-off dynamics are driven by rich rotation mechanisms around both the satellite and primary drops. The two pinch-off events create a small contracting liquid filament, characterized by local Oh ~ 0.05 and $L_{\text{ligament}}/R_{\text{ligament}} \sim 2.62$ and similar to those studied previously [56,57]. This small aspect ratio, in conjunction with the strong contracting kinetic energy derived from the second pinch-off, overcome capillary pressure forces to avoid an additional pinch-off instance in the small ligament. Observing the vorticity contours and the highlights at $\tilde{t} = 2.27$ – 2.37 , an example of a vortex ring detachment can be noticed at the forming neck of the filament, where the vorticity boundary layer detaches and advects towards the center of the bulbous region, pushing flow away from the neck and promoting the escape from pinch-off [49,58,59]. As seen in $\tilde{t} = 2.45$, succeeding the small liquid filament retraction in the counterflow direction ($\tilde{t} = 2.37$) we spot a counterexpansion (see positive $\tilde{\omega}_z$ at $\tilde{t} = 2.45$) that generates the bullet-like satellite drop depicted at $\tilde{t} = 2.51$ and that eventually coalesces with the primary drop. The process of incorporation of the satellite into the primary drop exhibits the progressive growth of the finite liquid bridge [60], driven by the two opposite-signed high $|\tilde{\omega}_x|$ rings in its vicinity (see $\tilde{t} = 2.98$) as well as complex dynamics of interfacial waves across the newly formed drop (see $\tilde{t} = 3.07$).

B. Influence of surfactant parameters on reentrant liquid jet formation and encapsulation dynamics

Having examined in detail the different encapsulation phenomena observed for high Ca in surfactant-free interfaces, we continue our analysis to explore the influence of key surfactant dimensionless groups. We begin by exploring the locality of the pinch-off in surfactant-free and surfactant-laden cases. We follow this by highlighting the influence of Marangoni stresses on the infiltration liquid shape, followed by describing the relative effect of β_s and Bi . Thereafter, we analyze the competition between the rates of interface surfactant adsorption and desorption, represented by k and Da simultaneously.

1. Focus on the pinch-off dynamics for surfactant-free and surfactant-laden cases

We examine in this subsection the locality of the reentrant jet breakup in our simulations and contrast the neck thinning behavior to that of the well-established theoretical scalings of Eggers [61] and Day *et al.* [62] for the minimum neck radius, r_{\min} , and its evolution over time, $t_p - t$, where t_p is the breakup time. We focus on the first observed breakup singularity for the surfactant-free case, which corresponds to a “back pinch-off” event, as defined in Sec. III A and Figs. 3(a) and 3(c) at $\tilde{t} = 0.99$ – 2.16 . Figure 4(a) contrasts the thinning progression of the pinching necks using the two mesh resolutions extensively tested in Appendix B (M1 and M2), along with an additional “medium” mesh with global resolution $M1.5 = 5376 \times 192 \times 192$. Figure 4(b) depicts zoomed-in snapshots, color coded by $\tilde{\omega}_z$, of the liquid jet as it approaches the singularity.

An inspection of this figure provides further evidence of the nearly complete independence of our results on the mesh resolution from M1 and beyond, as well as the robustness of our numerical approach, which is able to correctly capture the system’s universal dynamics at the scale of the pinch-off in terms of both thinning rate and scaling exponents. Reassuringly, we observe an

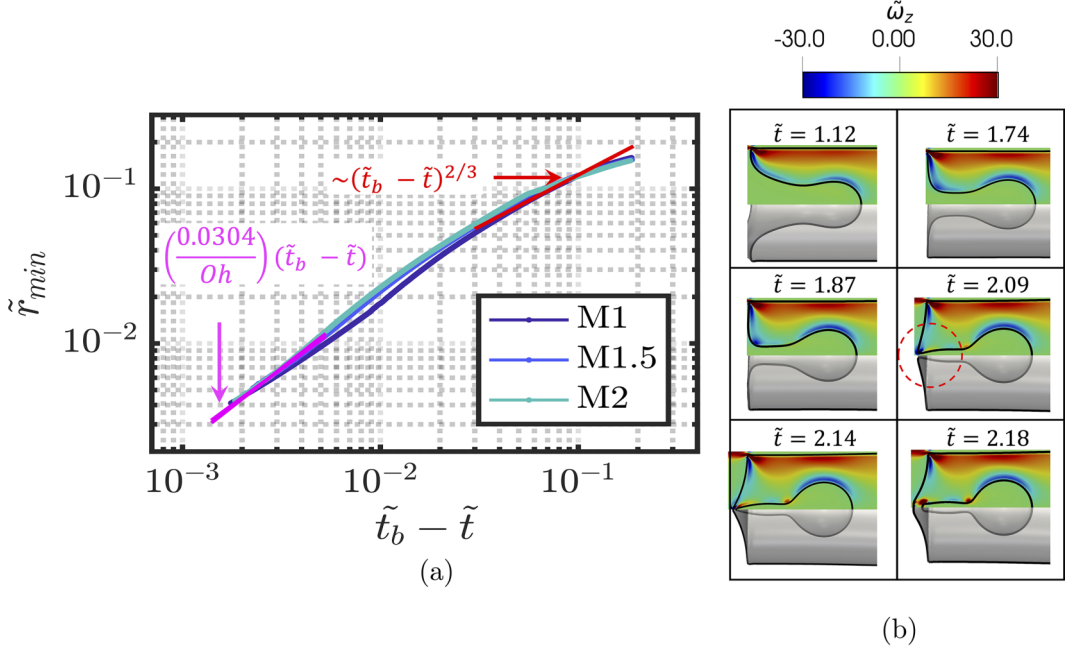


FIG. 4. Neck thinning analysis for the “back pinch-off” event of a surfactant-free interface. (a) Plot of the minimum neck radius, r_{\min} , vs the time before pinch-off, $t_p - t$, depicting how our simulations correctly retrieve the well-known inertial-viscous (pink line) pinching regime of Eggers [61] and approximate the inertial-capillary regime predicted by Day *et al.* [62]. Here the time has been scaled by the inertial-capillary timescale, $t_{\text{in-cap}} = \sqrt{\rho_l D^3 / \sigma_s}$. (b) Zoomed-in $\tilde{\omega}_z$ contour plots of the pinch-off. All other parameters remain unchanged from those specified in Sec. II B for the base case.

almost complete overlap of the curves for the three resolutions as $r_{\min}(t) \rightarrow 0$ ($\tilde{t}_b - \tilde{t} \lesssim 4 \times 10^{-3}$), where the universal scaling for the inertial-viscous (IV) regime of Eggers [61] [$r_{\min} \sim (t_p - t)$] is correctly recovered. At early thinning stages ($\tilde{t}_b - \tilde{t} \approx 2 \times 10^{-1} - 6 \times 10^{-2}$ in our systems), the competition between fluid inertia of the opposing capillary forces yields the inertial-capillary regime (IC [62], dictated by $r_{\min} \sim (t_p - t)^{2/3}$ and highlighted in red) for the liquid thread, which later transits into intermediate regimes, as predicted in Castrejón-Pita *et al.* [63]. It is important to note that although our obtained solution approximates the IC regime, it does not precisely match the theoretical preexponent of ≈ 0.7 [54] or the $2/3$ exponent proposed in Ref. [62]. For reference, the closest matches to the scaling were found to be $\tilde{r}_{\min} \approx 0.67(\tilde{t}_b - \tilde{t})^{2/3}$, $\tilde{r}_{\min} \approx 0.6(\tilde{t}_b - \tilde{t})^{0.62}$, and $\tilde{r}_{\min} \approx 0.55(\tilde{t}_b - \tilde{t})^{0.56}$ for M1, M1.5, and M2, respectively. Moreover, it can be noticed that the intermediate stages in our plot appear to be moderately sensitive to the resolution.

The above mentioned deviations from the theoretical scalings can be attributed to the dissimilarities between our system and those studied in Refs. [61,62]. Our system consists of a three-dimensional confined capillary channel wherein inertial effects are non-negligible, the pinching thread grows axially due to the action of the main flow, and the pinching domain remains in motion across the channel. These intricate dynamics are not accounted for in the theoretical scalings, which were initially proposed in an axisymmetric context under free-flow conditions. It is these dissimilarities between our system and the theoretical framework that likely contribute to the observed discrepancy between our solution and the IC regime. As mentioned in our previous work [49,50], the nature of our 3D simulations makes it prohibitively difficult to capture the dynamic intermediate regimes reported in Castrejón-Pita *et al.* [63], a fact that likely explains the deviations found between mesh resolutions at intermediate times.

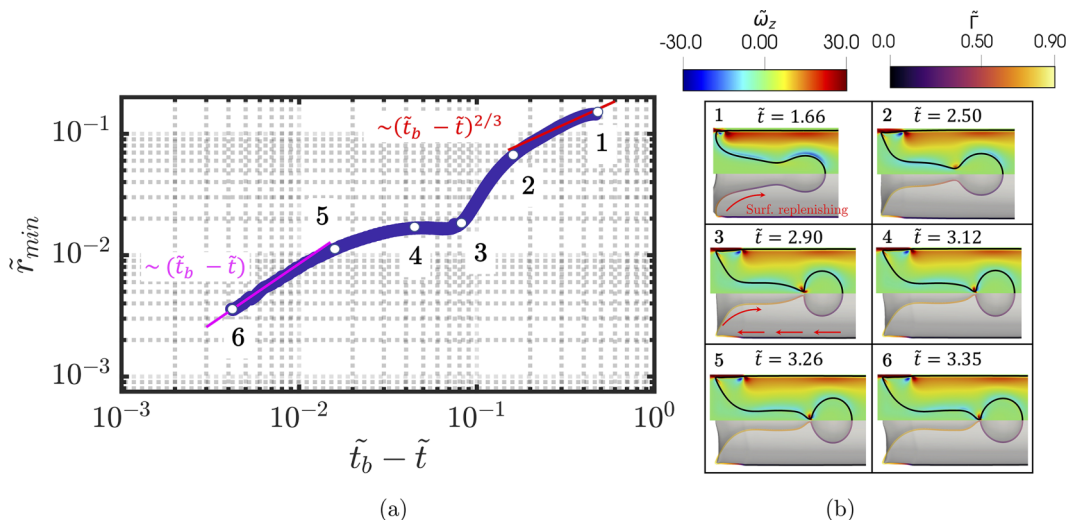


FIG. 5. Neck thinning analysis for the “interior pinch-off” event of a surfactant-laden case characterized by $k = 0.25$ ($Da = 0.4$). (a) Plot of the minimum neck radius, r_{\min} , vs the time before pinch-off, $t_p - t$, depicting how our simulations correctly retrieve the well-known inertial-capillary (red line) and inertial-viscous (pink line) pinching regimes predicted by Eggers [61] and Day *et al.* [62], and the occurrence of three intermediary regimes. Here the time has been scaled by the inertial-capillary timescale, $t_{\text{in-cap}} = \sqrt{\rho_l D^3 / \sigma_s}$. (b) Zoomed-in $\tilde{\omega}_z$ (top) and $\tilde{\Gamma}$ (bottom) contour plots of the pinch-off. All other parameters remain unchanged from those specified in Sec. II B for the base case.

We further investigate the pinching phenomenon of our system by tracking the reentrant jet breakup process in the presence of surfactants. To do so, we take as a case study the first “interior pinch-off” event of a simulation run characterized by $k = 0.25$ ($Da = 0.4$), with the remaining parameters kept constant from those ascribed to the base case in Sec. II B. The results from this analysis are summarized in Fig. 5. Remarkably, these results are in agreement with the existing literature on surfactant-covered liquid thread breakup surrounded by a static gas phase (see, for example, Craster *et al.* [64], Kamat *et al.* [65], Liao *et al.* [66], Wee *et al.* [67], Xu *et al.* [68]); our surfactant-laden system, which is characterized by a moving liquid jet in confined flow with non-negligible inertia, adheres to a breakup mode in the inertial-viscous regime of Eggers [61] as $r_{\min}(t) \rightarrow 0$ and to the inertial-capillary regime in the early thinning stages, akin to our observations for the surfactant-free case. As reported well in the references provided above, at the locality of the pinch-off, the competing inertial, viscous, capillary, and Marangoni-related forces balance in a way that makes the thinning neck evolve as if there were no surfactants present, even if large Marangoni stresses arise near the pinching point to reopen the neck [65]. The intermediary dynamics between that characterized by the $(\tilde{t}_b - \tilde{t})^{2/3}$ and $(\tilde{t}_b - \tilde{t})$ scalings, however, is influenced by the presence of surfactant. The existence of intermediary scalings that eventually lead to the inertial-viscous regime has been reported previously in Xu *et al.* [68] for small Pe and seen in Kamat *et al.* [65] and Wee *et al.* [67], for $Pe \rightarrow \infty$ (see Fig. 5 of the first reference). This is illustrated in Fig. 5(b) where the lower half of the jet is coloured by interfacial surfactant concentration, $\tilde{\Gamma}$. Due to the confinement effects present in our system, the bulk flow in the axial direction drags surfactants from their accumulation zones at the bubble’s rear and distributes them along the liquid jet. In our system, this action appears to counteract the surfactant depletion process at the pinching point typically reported in surfactant-covered capillary breakup [64,67].

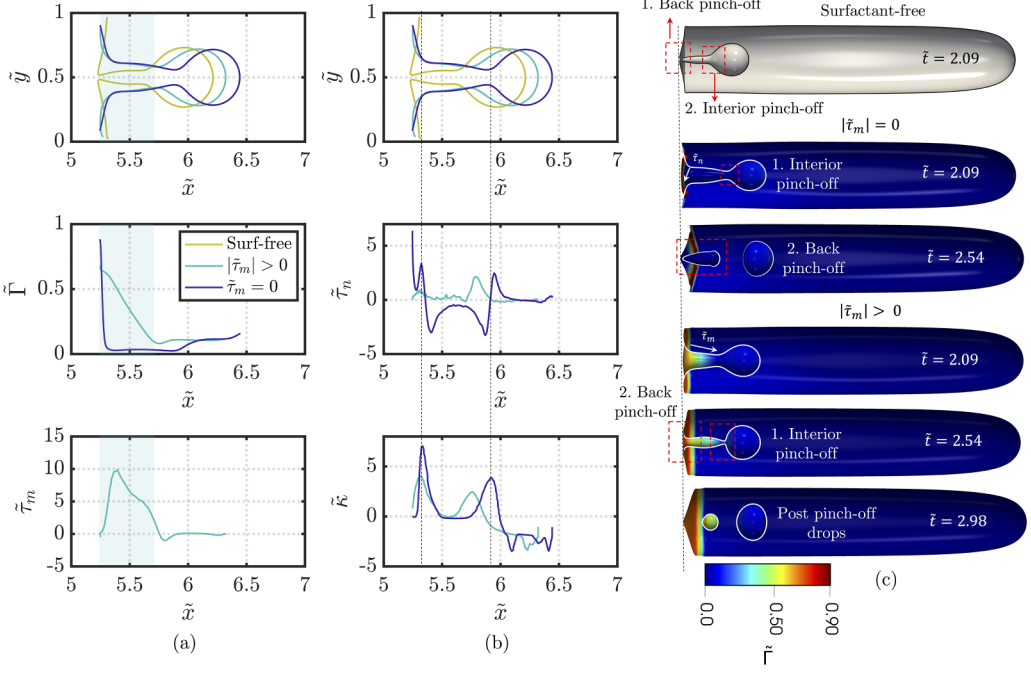


FIG. 6. Effect of Marangoni stresses on reentrant liquid jet formation and encapsulation. (a) Liquid-filled jet shape (top), surfactant interfacial concentration (middle), and Marangoni stresses (bottom). (b) Liquid-filled jet shape (top), normal stresses (middle), and interface curvature (bottom). $|\tilde{\tau}_m| > 0$ corresponds to Marangoni-supported, while $|\tilde{\tau}_m| = 0$ to Marangoni-free. Plots of two-dimensional projection in the x - y plane ($\tilde{z} = 0.5$) and at $\tilde{t} = 2.09, 2.10, 2.11$ for surfactant-free $|\tilde{\tau}_m| = 0$, and $|\tilde{\tau}_m| > 0$, respectively. (c) 3D schematic of pinch-off mechanisms. The interfaces of these images have been slightly translated in the x direction to have a common point of reference (marked by the black dotted line); for their real location in the channel, refer to (a, top). $\tilde{t}_{p-o,bk} = 2.16, 2.55, 2.90$ and $\tilde{t}_{p-o,int} = 2.33, 2.37, 2.62$ for surfactant-free, $|\tilde{\tau}_m| = 0$, and $|\tilde{\tau}_m| > 0$, respectively. All other parameters remain unchanged from those specified in Sec. II B for the base case.

2. Marangoni stresses, surface elasticity, and Biot number

Here we elucidate the behavior of a surfactant-laden system under the conditions ascribed to the “base” case (refer to Sec. II B) and compare it to that of clean interfaces. To isolate the effects of lower surface tension from those arising from Marangoni stresses on the encapsulation dynamics, we have set up an additional case, denoted by $|\tilde{\tau}_m| = 0$, in which we have suppressed the last term on the r.h.s. of Eq. (2) to inhibit Marangoni stresses while simultaneously allowing the reduction of surface tension. Figures 6(a) and 6(b) show the shape of the liquid jet and a few other characteristics along its interface at $\tilde{t} = 2.09 - 2.11$. We have duplicated the plots of interfacial shape on both column panels for clarity. Examination of the plots uncovers an almost surfactant-free interface at the liquid jet for $|\tilde{\tau}_m| = 0$, which exhibits a significant drop in $\tilde{\Gamma}$ going from the edge to the interior of the reentrant jet in the streamwise direction and a slight surge after surpassing the incipient pinching neck. This rapid loss of surfactant for $|\tilde{\tau}_m| = 0$, as opposed to the Marangoni-supported case, $|\tilde{\tau}_m| > 0$, is explained by noticing that the base case’s operating conditions promote surfactant desorption (large Da and small k) as $\tilde{\Gamma} \rightarrow 1$ [see Eq. (6)] as well as slow interface surfactant diffusion (large Pe_s). Reverting to the remarks by Batchvarov *et al.* [27] and Atasi *et al.* [39], the motion of the bubble prompts surfactant accumulation at the back due to drag forces from the liquid phase, partially counteracted by Marangoni stresses in the opposite direction for $|\tilde{\tau}_m| > 0$. The

absence of Marangoni stresses in the $|\tilde{\tau}_m| = 0$ case leads to a continuous process of local surfactant accumulation at the back and desorption into the bulk, depleting the interface of surfactants.

Figure 6(c) portrays a key difference in the encapsulation behavior between the three cases, where the succession of back pinch-off first and interior pinch-off second observed for clean interfaces is reversed in the presence of surfactants and the overall pinch-off dynamics are delayed (see the figure caption for the pinch-off times). This delay is accentuated for $|\tilde{\tau}_m| > 0$, as can be observed from the local peaks in $\tilde{\kappa}$ and $\tilde{\tau}_n$ of Fig. 6(b), which, in the case of $|\tilde{\tau}_m| = 0$, are already pulling the interface towards the channel center, signaling the onset of capillary neck closure. Part of the role of Marangoni stresses can be seen in the green-shaded region of Fig. 6(a), where these tangential stresses counteract capillary forces at both the back and interior pinch-off regions. These observations are in complete agreement with Refs. [49,65,69] for liquid threads, although we note that in our system the Marangoni forces exerted on the interface are not sufficient to escape pinch-off completely. The inversion of back and interior pinch-off times in contaminated interfaces can be attributed to the noticeably nonuniform surfactant distribution along the liquid jet, which displays its highest values in the regions neighboring the capillary neck at the back of the jet, lowering surface tension and providing additional disruption to neck closure in comparison to the interior neck.

The effect of the surfactant-induced interior and back pinch-off delays can be further described through the evolution of the satellite drop, illustrated in Fig. 6(c) for $|\tilde{\tau}_m| > 0$. Unlike its surfactant-free counterpart (see Fig. 3(c), $\tilde{t} = 2.37-2.98$), this satellite drop does not recombine with the main drop before the bubble reaches the end of the channel domain in our simulations. Nevertheless, we note that the satellite drop's average velocity exceeds that of the main drop by about 30% under the conditions displayed in Fig. 6(c), suggesting an eventual drop coalescence in an extended channel. In surfactant-laden scenarios, the delayed coalescence of drops is attributed to the reentrant jet's lower surface tension, allowing faster infiltration into the bubble due to reduced resistance to liquid flow. This, in combination with Marangoni stresses opposing the jet's breakup, causes a delay in the back and interior pinch-off events and increases the spatial separation between the main and satellite drop. Measurements at $\tilde{t} = 2.66$ reveal a dimensionless distance ($\tilde{d}_{\text{main,sat}}$) of 0.13 for surfactant-free cases and 0.31 for the surfactant-laden case depicted in Fig. 6(c). We note that the formation of the satellite drop is confined to surfactant-laden cases with highly desorptive characteristics, as explained in Sec. III C.

For the first part of our parametric investigation, we study the effect of β_s on encapsulation and the post-pinch-off dynamics. As Fig. 7(a) depicts, and in line with previous studies in the context of ink-jet printing [70,71], increasing surfactant strength gradually increases the speed of liquid infiltration and decreases the rate of neck thinning at both the back and interior of the reentrant jet [see locations of jet nose in Fig. 7(a) and pinch-off times in the figure caption]. This delay is materialized in the larger $|\tilde{\kappa}|$ peaks seen for $\beta_s = 0.25$ at the incipient pinching necks, as well as the higher $|\tilde{\tau}_m|$ that arise at their vicinity, seeking to counteract capillary draining [72]. Figure 7(b) illustrates the progression of the primary encapsulated drop as it travels across the bubble domain in the form of its volume-averaged x velocity, $u_{x,d}$, normalized by U_b (top), interfacial area, A_d , normalized by its area after pinch-off, $A_{d,0}$ (middle), and ratio between drop length in the x and y directions, a/b (bottom). The encapsulated drops exhibit three common characteristics irrespective of the presence of surfactants, namely, a higher streamwise velocity than the bubble nose, highlighting the potential for a scenario in which the bubble nose interface is ruptured by the drop, an overall decrease in interfacial area, and dampening a/b oscillations in time, which culminate in virtually spherical drops. This bubble nose rupture is further analyzed in Sec. III C. Under the conditions considered, the addition of a strong surfactant ($\beta_s = 1$) decreases the rate of surface area reduction and significantly increases drop velocity relative to the bubble nose. The nonmonotonic behavior of $u_{x,d}/U_b$ with regard to a clean interface and weak surfactants ($\beta_s = 0.25-0.50$) can be explained by observing in Fig. 7(c) the spatial distribution of $\tilde{\Gamma}$, $\tilde{\sigma}$, and $\tilde{\tau}_m$ in the encapsulated drop at $\tilde{t} = 7.70$. Despite the largest $|\tilde{\tau}_m|$ opposing drop propagation in the streamwise direction for the strongest surfactant, it is seen that these effects are fully countered by the lower surface tension across the drop's domain, yielding a higher drop velocity than the surfactant-free case. In contrast, the weak

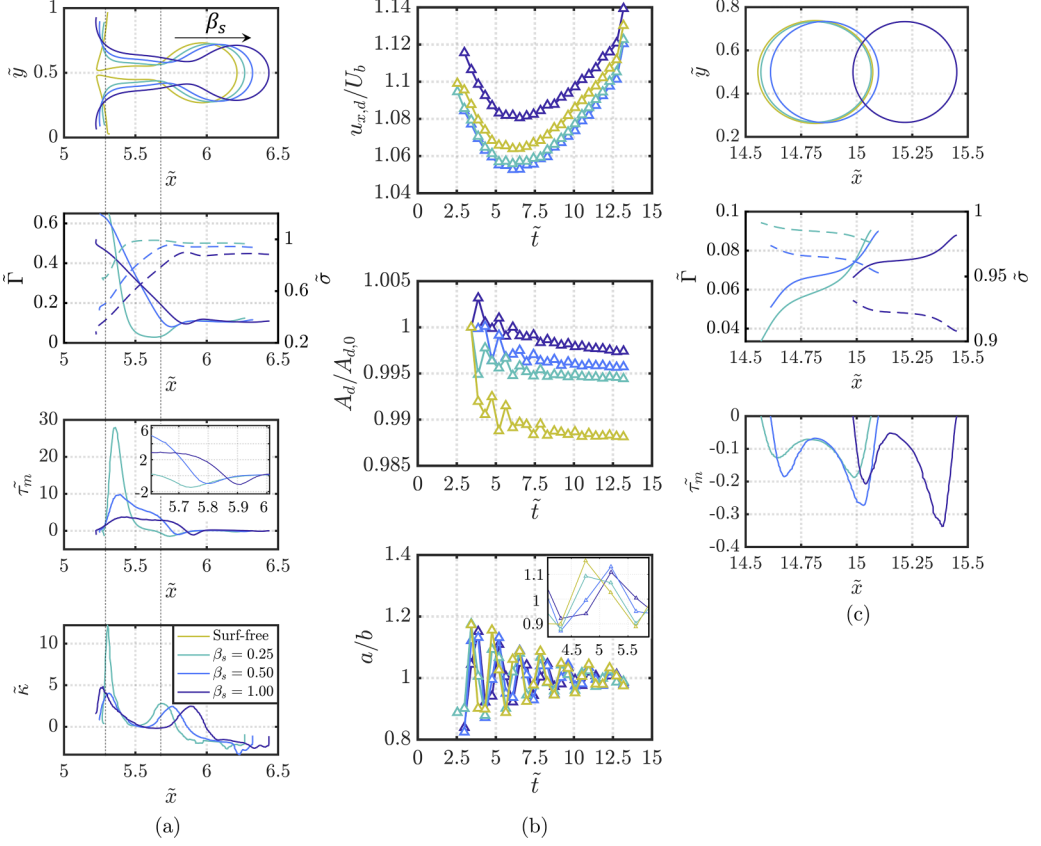


FIG. 7. Effect of β_s on reentrant liquid jet formation and encapsulation. (a) Liquid-filled jet shape, surfactant interfacial concentration (left axis, continuous line), and surface tension (right axis, dotted line), Marangoni stresses, and interface curvature at $\tilde{t} = 2.09, 2.10, 2.10, 2.09$ for surfactant-free and $\beta_s = 0.25, 0.50, 1$, respectively. (b) Temporal evolution of primary encapsulated drop velocity normalized by bubble velocity, primary drop interfacial area normalized by area after pinch-off, and ratio between drop length in the x and y directions. Data points computed for all cases every 10^{-3} s. (c) Primary encapsulated drop shape, surfactant interfacial concentration (left axis, continuous line), and surface tension (right axis, dotted line) and Marangoni stresses at $\tilde{t} = 7.70$. Plots on two-dimensional projection in the x - y plane ($\tilde{z} = 0.5$) for (a), (c). $\tilde{t}_{p-o,bk} = 2.16, 2.52, 2.90, 3.83$ and $\tilde{t}_{p-o,int} = 2.33, 2.40, 2.62, 2.77$ for surfactant-free and $\beta_s = 0.25, 0.50, 1$, respectively. All other parameters remain unchanged from those specified in Sec. II B for the base case.

surfactant cases feature an almost clean interface with surface tension values very close to the clean case, but with nonzero Marangoni effects that induce a delay in drop propagation.

The morphological deformations that characterize drop behavior after pinch-off, as depicted in Fig. 7(b) (bottom), demonstrate the presence of a semiperiodic oscillating pattern monotonically influenced by surface elasticity. In the inset of this figure, a higher deviation from a fully spherical drop can be appreciated for the surfactant-free case in both the major crests and troughs of the oscillatory structures. Considering these results, we draw parallels with the study of Wang *et al.* [73] in an ink-jet system, whose main results suggest that the extent of deformation decreases with Ca (after a critical Ca has been reached), in line with our numerical observations for increasing β_s . Estimating the frequency of a/b oscillations through the classic expression of Rayleigh [74] ($f \sim \sqrt{\sigma/\rho_c r_d^3}$, where r_d is the drop's spherical equivalent radius) at the latest time recorded ($\tilde{t} \approx 13.17$), we obtain $\tilde{f} \sim 1.49, 1.55, 1.55, 1.57$ for surfactant-free and $\beta_s = 0.25, 0.50, 1$,

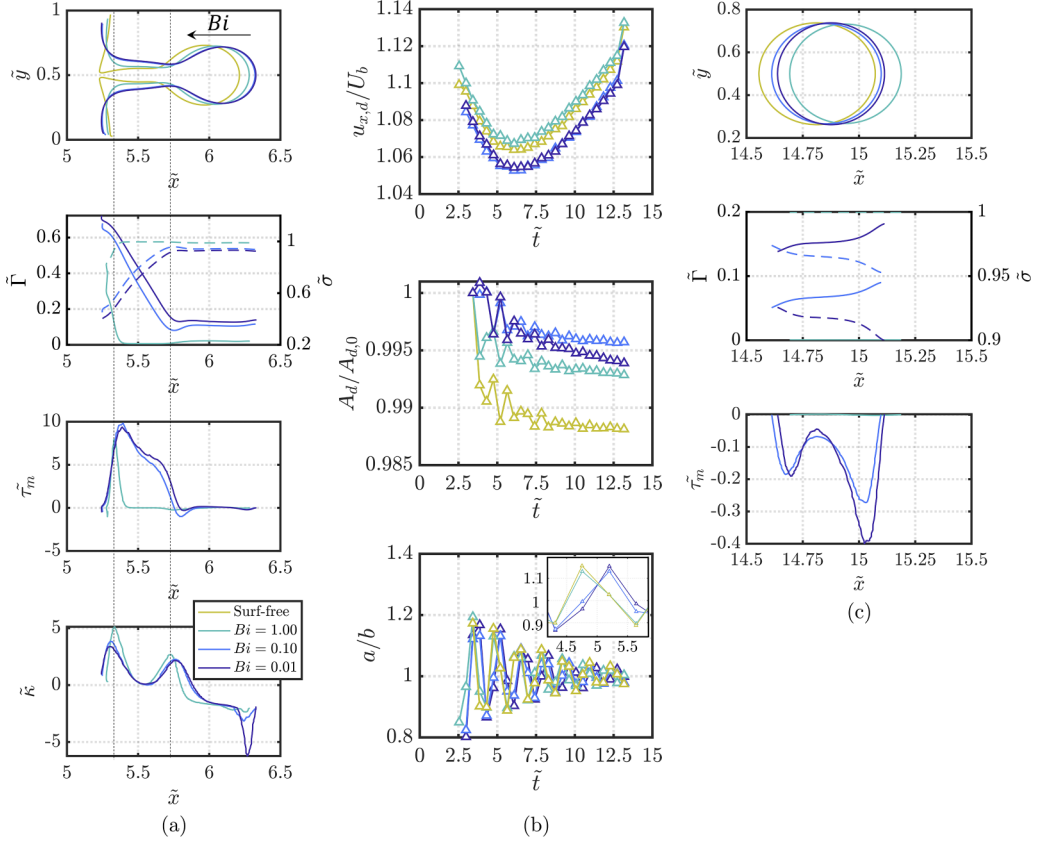


FIG. 8. Effect of Bi on reentrant liquid jet formation and encapsulation. (a) Liquid-filled jet shape, surfactant interfacial concentration (left axis, continuous line), and surface tension (right axis, dashed line), Marangoni stresses, and interface curvature at $\tilde{t} = 2.09, 2.10, 2.10, 2.10$ for surfactant-free and $Bi = 1, 0.10, 0.01$, respectively. (b) Temporal evolution of primary encapsulated drop velocity normalized by bubble velocity, primary drop interfacial area normalized by area after pinch-off, and ratio between drop length in the x and y directions. Data points computed for all cases every 10^{-3} s. (c) Primary encapsulated drop shape, surfactant interfacial concentration (left axis, continuous line), surface tension (right axis, dashed line), and Marangoni stresses at $\tilde{t} = 7.70$. Plots of two-dimensional projection in the x - y plane ($\tilde{z} = 0.5$) for (a), (c). $\tilde{t}_{p-o,bk} = 2.16, 2.63, 2.90, 3.09$ and $\tilde{t}_{p-o,int} = 2.33, 2.37, 2.62, 2.68$ for surfactant-free and $Bi = 1, 0.10, 0.01$, respectively. All other parameters remain unchanged from those specified in Sec. II B for the base case.

respectively, implying a dominating effect of lower drop radius over lower surface tension on the frequency of deformation cycles for increasing β_s .

The effects arising from altering Bi in the range 0.01–1 are depicted in the plots of Fig. 8. An interface covered by a highly soluble surfactant (i.e., high Bi) undergoes rapid rates of mass exchange between the interface and bulk as a result of its comparatively low (high) characteristic desorptive (inertial) time. This is demonstrated by noticing the significantly lower $\tilde{\Gamma}$ distributed along the liquid jet for the highest Bi considered, which, barring the surfactant-free case ($Bi \rightarrow \infty$), exhibits the slowest rate of jet formation and the fastest pinch-off events [see location of jet nose in Fig. 8(a) (top) and figure caption for the pinch-off times]. Similar to our previous remarks, the signature $|\tilde{\tau}_m|$, $|\tilde{\kappa}|$, and capillary pressure peaks (not shown) that signal the onset of capillary neck closure and the advent of pinch-off are already developing in a noticeable manner for $Bi = 1$, in contrast to $Bi = 0.01$ – 0.10 . The post-pinch-off temporal evolution of the primary drop, as depicted

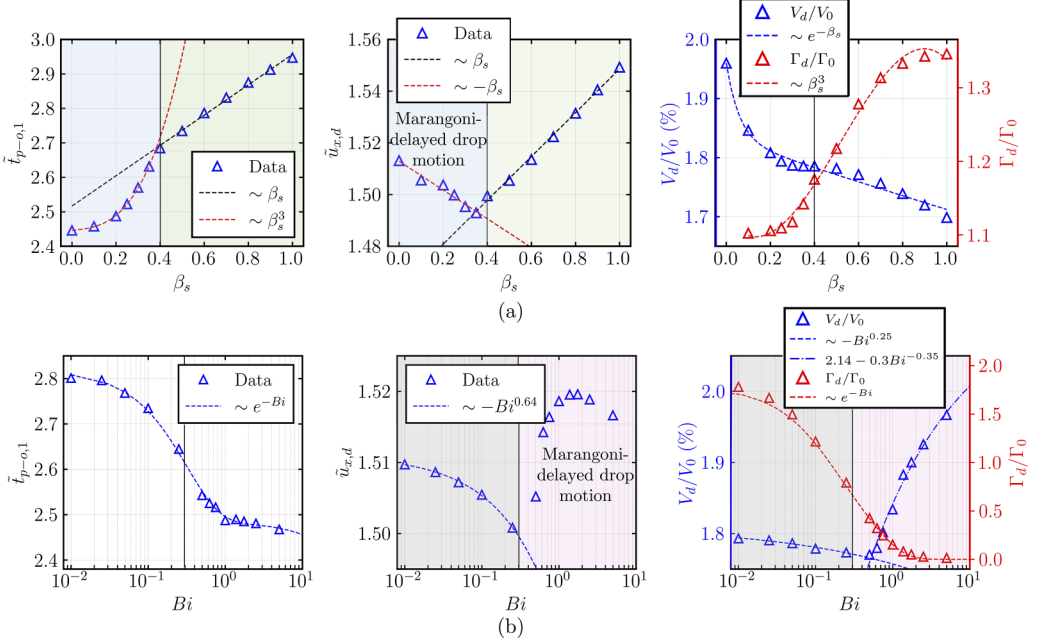


FIG. 9. Impact of surfactant parameters on pinch-off dynamics and evolution of first encapsulated drop for a highly desorptive surfactant ($k = 0.1$). (a) Effect of β_s at $Bi = 0.1$. (b) Effect of Bi at $\beta_s = 0.5$. All other parameters remain unchanged from those specified in Sec. II B for the base case.

in Fig. 8(b), reveals similar trends to those referenced in the above analysis of β_s in terms of drop shrinkage, its attenuation in surfactant-laden cases, and semiperiodic drop size oscillations.

Figure 9 elucidates the functional relationships that interlink β_s and Bi to key outcomes characterizing the encapsulating system. These outcomes encompass the first pinch-off event ($\tilde{t}_{p-o,1}$), the post-detachment volume-averaged drop velocity ($\tilde{u}_{x,d}$), the first encapsulated drop's volume (normalized by the bubble's initial volume, V_d/V_0), and the drop's interface surfactant concentration (normalized by the initial concentration, Γ_d/Γ_0). The figure incorporates best-fit curves for each variable for reference. An examination of the relationships pertaining to β_s in Fig. 9(a) unveils a distinct divergence between behavioral modes for $\beta_s < 0.4$ (highlighted in blue) and $\beta_s \geq 0.4$ (highlighted in green). This divergence is particularly evident for $\tilde{t}_{p-o,1}$ and $\tilde{u}_{x,d}$. In the latter β_s range, well-established surfactant-induced effects, discussed in this paper and widely reported in the literature, come to the forefront. These include the concurrent impact of stabilizing Marangoni stresses and reduced local surface tension (i.e., increase in local Oh) contributing to thwart/delay capillary breakup and reduce drop size, as previously reported in Refs. [65,69,75].

Our simulation results reveal that a surface elasticity surge (maintaining all other dimensionless groups unchanged) brings about the generation of encapsulated drops of increasing surfactant concentration and smaller size (see plots of Γ_d/Γ_0 and V_d/V_0). A larger Γ/Γ_0 , in tandem with an augmented sensitivity of $\tilde{\sigma}$ to $\tilde{\Gamma}$ for increased β_s [indicated by the Langmuir relation in Eq. (7)] point to lower $\tilde{\sigma}$ during the reentrant jet infiltration and pinch-off events. In fact, applying the Langmuir relation to the Γ_d/Γ_0 data of Fig. 9(a), we find that $\tilde{\sigma}$ ranges from 1 to 0.869 for $\beta_s = 0$ and $\beta_s = 1$, respectively. Coupling this analysis with the understanding that $|\tau_m| \sim \beta_s$ (see Sec. II A), it is possible to rationalize the direct relationship between $\tilde{t}_{p-o,1}$ and β_s by invoking the above mentioned compounded action of larger Marangoni stresses and lower surface tension to resist capillary breakup for larger values of β_s .

The direct relationship registered between $\tilde{u}_{x,d}$ and β_s for $\beta_s \geq 0.4$, featuring a linear growth under our studied conditions, owes its behavior to the diminished capillary resistance to liquid infiltration into the bubble's domain, as mentioned previously in Sec. I. This directly proportional response of $\tilde{u}_{x,d}$ to β_s is akin to the well-established links between velocity of drops formed through end pinching and Oh ($\sim \sigma^{-1/2}$, precipitated by larger β_s in our simulations, as previously explained) in the problem of jet droplets released to the atmosphere through bursting bubbles [76]. The inversely monotonic $\tilde{u}_{x,d}$ vs β_s relationship, evident for $\beta_s < 0.4$, embodies the nuanced effects of surface tension and Marangoni stresses, as briefly discussed in our analysis of Fig. 7. The uneven distribution of surfactant across encapsulated drops [larger concentration at the drop's nose; refer to Fig. 7(c), bottom] instigates counterflow Marangoni stresses ($\tilde{\tau}_{m,x} < 0$), hindering the motion of the drop. These Marangoni stresses, though small, are non-negligible, constituting approximately 10% of the Marangoni forces exerted on the infiltrating jet prior to pinch-off (see Fig. 7). For instances where $\beta_s < 0.4$, the anticipated acceleration of the drop due to reduced surface tension is offset by these Marangoni stresses, thereby resulting in a slightly decreased drop velocity with increased surfactant strength.

The parameter sweep of surfactant solubility elucidated in Fig. 9(b) mirrors that of β_s in the discernible emergence of dual behavioral modes, this time noticeable for $\tilde{u}_{x,d}$ and V_d/V_0 and clearly separated by $\text{Bi} \approx 0.30$. Before understanding this duality (highlighted in gray and magenta), we examine the expected behavior detected for $\tilde{t}_{p-o,1}$ and Γ_d/Γ_0 . Both variables conform to a conspicuous exponential decline with increased Bi. This signals that elevated rates of mass transfer between the interface and the bulk compared to convection—indicative of enhanced solubility or larger Bi—predominantly deplete the interface of surfactant and concurrently accelerate capillary breakup with respect to lower Bi. Notice that these cases correspond to $k = t_{\text{des}}/t_{\text{ad}} = 0.1$, stipulating that surfactant desorption is heavily promoted over adsorption, leading to the high-rate plummeting of $\tilde{\Gamma}/\tilde{\Gamma}_0$ with Bi and the roughly surfactant-free drops observed for $\text{Bi} > 1$ ($\tilde{\sigma} \approx 1 - 0.08e^{-3.81\text{Bi}}$, not shown in the plot). The inverse exponential dependence recovered for $\tilde{t}_{p-o,1}$ and Γ_d/Γ_0 imposes explicit bounds for these values between the two limiting cases: surfactant-free ($\text{Bi} \rightarrow \infty$, $\tilde{t}_{p-o,1} = 2.48$ and $\Gamma/\Gamma_0 = 0$) and insoluble surfactant ($\text{Bi} = 0$, $\tilde{t}_{p-o,1} = 2.81$ and $\Gamma/\Gamma_0 = 1.87$). The approximately twofold increase in drop surfactant concentration with respect to initial surfactant coverage as the insoluble limit is approached is consistent with other applications. For instance, in the context of jet drops formed via bursting bubbles, Ref. [77] reports a 1.6 times increase in $\tilde{\Gamma}$ of the released drops with respect to that of the equilibrated bubble interface before bursting.

Focusing on the behavioral divergence obtained for $\text{Bi} \approx 0.3$, an inverse relation between V_d/V_0 and Bi is recovered for $\text{Bi} > 0.3$. In a similar fashion to the trends elucidated for surface elasticity, the diminished $\tilde{\sigma}$ associated with augmented surfactant coverage as Bi decreases generates smaller encapsulated drops. As we venture into the $\text{Bi} \lesssim 0.3$ territory, a pronounced plunge in the sensitivity of V_d/V_0 to Bi is identified with respect to that of $\text{Bi} > 0.3$. The $\text{Bi} < 0.3$ range adheres to $|d(V_0/V_d)/d\text{Bi}| = -0.0125\text{Bi}^{-3/4}$, whereas $\text{Bi} > 0.3$ is driven by $|d(V_0/V_d)/d\text{Bi}| = 0.105\text{Bi}^{-1.35}$ [one to two orders of magnitude larger $|d(V_0/V_d)/d\text{Bi}|$ for $\text{Bi} > 0.3$ within the entire Bi range studied]. This analysis hints at a saturation of surfactant effects for increasingly insoluble contaminants. To finalize the present discussion of Fig. 9, we call attention to the similar behavior of $\tilde{u}_{d,x}$ in $\text{Bi} > 0.3$ as that in $\beta_s < 0.4$, that is, a neutralization of the drop acceleration effects introduced by lower surface tension (prompted by larger β_s or smaller Bi) by counterflow Marangoni stresses ($\tilde{\tau}_{m,x} < 0$).

3. Effect of surfactant adsorption/desorption kinetics (Da and k)

We now proceed to examine the influence of directly contrasting the characteristic times of adsorption and desorption, along with the initial interface saturation through varying k and Da simultaneously. This concurrent variation allows us to maintain all other parameters constant. Figure 10(a) portrays a monotonic response of the liquid infiltration depth and $\tilde{\Gamma}$ with k and Da , where the rapid rates of surfactant adsorption inherent to the high k (low Da) cases are materialized

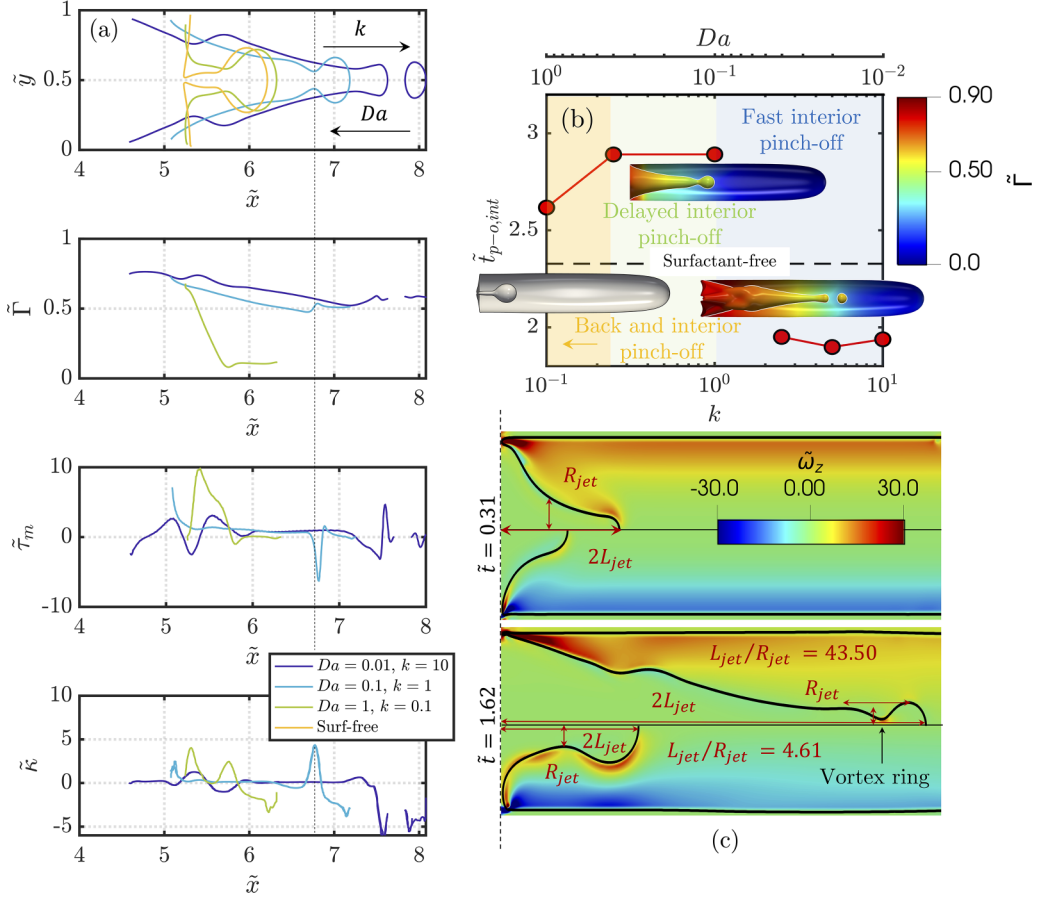


FIG. 10. Effect of k and Da on reentrant liquid jet formation and encapsulation. (a) Liquid-filled jet shape, surfactant interfacial concentration, Marangoni stresses, and interface curvature at $\tilde{t} = 2.09, 2.10, 2.09, 2.09$ for surfactant-free and $k = 0.1, 1, 10$, respectively. (b) Interior pinch-off time vs k and Da , and schematic of the three regions that divide thinning behavior. (c) Contour plots of normalized vorticity in the z direction and comparison of infiltrating liquid shape for $k = 10.0, Da = 0.01$ (top), and $k = 0.1, Da = 1.0$ (bottom). The interfaces of these contour plots have been translated in the x direction to have a common point of reference (marked by the black dotted line). Plots on two-dimensional projection in the x - y plane ($\tilde{z} = 0.5$). All other parameters remain unchanged from those specified in Sec. II B for the base case.

in the relatively large and comparatively constant $\tilde{\Gamma}$ distributions along the reentrant jet. In line with our previous results, general reductions in local surface tension at the bubble rear, brought about by higher k or β_s and lower Bi conditions, promote a faster and deeper infiltration of liquid into the bubble domain. In Fig. 10(b) we record the time until the first pinch-off instance at the bubble interior as a function of k for the entire parameter space explored. A retardation of the capillary instabilities that lead to end pinching is seen as k is increased in the range $0 < k < 1$, consistent with our previous remarks about the combined effect of $\tilde{\sigma}$ and Marangoni stresses on opposing drop encapsulation. This behavior is mirrored by the $\tilde{\tau}_m$ and $\tilde{\kappa}$ peaks exposed near the nascent pinching necks for the lowest k cases displayed in Fig. 10(a) ($k = 0.1$ – 1.0), while the oscillations seen for $k = 10$ correspond to capillary waves in the infiltrating liquid, reported by Constante-Amores *et al.* [49] for long liquid ligaments.

Similar to our previous analyses of β_s , Bi, and Marangoni-free case for $k = 0.10$, it is found that increasing k in the range $k < 0.10$ results in a sequence inversion of the two main pinch-off events ($\tilde{t}_{p-o,bk} > \tilde{t}_{p-o,int}$) identified in clean interfaces ($\tilde{t}_{p-o,bk} < \tilde{t}_{p-o,int}$; see caption of Fig. 10). Interestingly, it is also found that for all cases above $k = 0.25$, the large accumulation of surfactants near the bubble rear provides a strong resistance to capillary pressure buildup in those regions, resulting in the partial elimination of the “back pinch-off” event until bubble bursting events occur. This will be further discussed in the following section. Another notable feature to highlight from Fig. 10(b) is the sharp decrease in $\tilde{t}_{p-o,int}$ above the critical value of $k = 1$. This discontinuity in the function $\tilde{t}_{p-o,int}$ vs k in conjunction with our observations about the elimination of the back pinch-off suggests a partition of the encapsulation dynamics into two major regions according to the rates of adsorption/desorption: (i) the above described region for $k < 1$, in which the presence of surfactants exerts a stabilizing effect, leading to a delay in neck thinning in relation to a fully clean interface, and (ii) a region of rapid liquid-filled jet formation in the axial direction alongside a significant acceleration of the first interior pinch-off event for $k > 1$. The first region is further segregated by the occurrence ($k < 0.25$, region i.a) or elimination ($k > 0.25$, region i.b) of the back pinch-off. An explanation for the marked transition from the first to the second region in terms of thinning rates is as follows. A general increase of surfactant coverage due to high rates of adsorption introduces high rates of viscous and inertial deformation to the interface, as noted by Bazhlekov *et al.* [78], hence increasing the axial velocity of the infiltrating liquid and its aspect ratio. Recalling the observations of Wang *et al.* [59] and Ambravaneswaran and Basaran [72] in contracting/expanding liquid filaments, we show in Fig. 10(c) how in cases above the critical k , L_{jet}/R_{jet} surpasses a given threshold value to enter the breakup regime and accelerate end pinching, even if the local values of surface tension are lower than those of smaller k conditions.

C. Bubble bursting, back deformations, and regime maps

This section provides a more detailed account of the post pinch-off dynamics, focusing specifically on the process of bubble bursting via the liquid jet/entrapped drops and the temporal fate of the bubble back and accompanying trailing structures. In Figs. 11(a) and 11(b) we summarize the three main bursting behaviors observed in the β_s - k and Bi- k (Da) spaces, leaving all other conditions specified in the baseline case unchanged. As captured in the figure, a first regime (I), distinctly bounded by a surfactant-free interface and k below the critical value defined in the previous section, is identified for all β_s and Bi tested. This regime adheres to a behavior mode of slow infiltration of liquid, monotonic delay of the first interior pinch-off event with increasing (decreasing) β_s (Bi) (see Fig. 9), and most importantly, eventual restoration of the interfacial morphology of the bubble back, depicted in Fig. 11(c), top. This restoration ensures a pseudo-stable entrapment of one or multiple drops of varying size and $\tilde{\Gamma}$ within the bubble domain, disrupted only by a potential rupture of the bubble nose by the first drop. We note that this rupture was not observed for any of the cases encompassed within (I) given the channel length employed in our simulations and the significant elongation of the bubble across the channel. The stability of the encapsulated drops-bubble compound in regime I poses a potential avenue for future research.

A second regime (II) emerges as k approaches the critical value, where a much faster and deeper liquid jet develops across the bubble and, ensuing from diminished capillary forces, further delays to pinch-off are recorded. These delays lead to the entrapment of the first drop in regions approaching the bubble nose in the axial direction, promptly leading to its rupture, as illustrated at $\tilde{t} = 5.19$ in Fig. 11(c), middle. Following a series of end-pinching events, the liquid jet undergoes several instances of escapes of pinch-off, in conjunction with a surge of surface capillary waves across its domain, and a radial growth that gives rise to a large bulbous end (see $\tilde{t} = 8.73$). These mechanisms are closely related to the intricate phenomena stemming from retracting liquid filaments, as addressed in Refs. [49,79]. This substantial growth causes the liquid jet to burst the interface near the channel walls, thereby fully separating the original bubble into two individual entities.

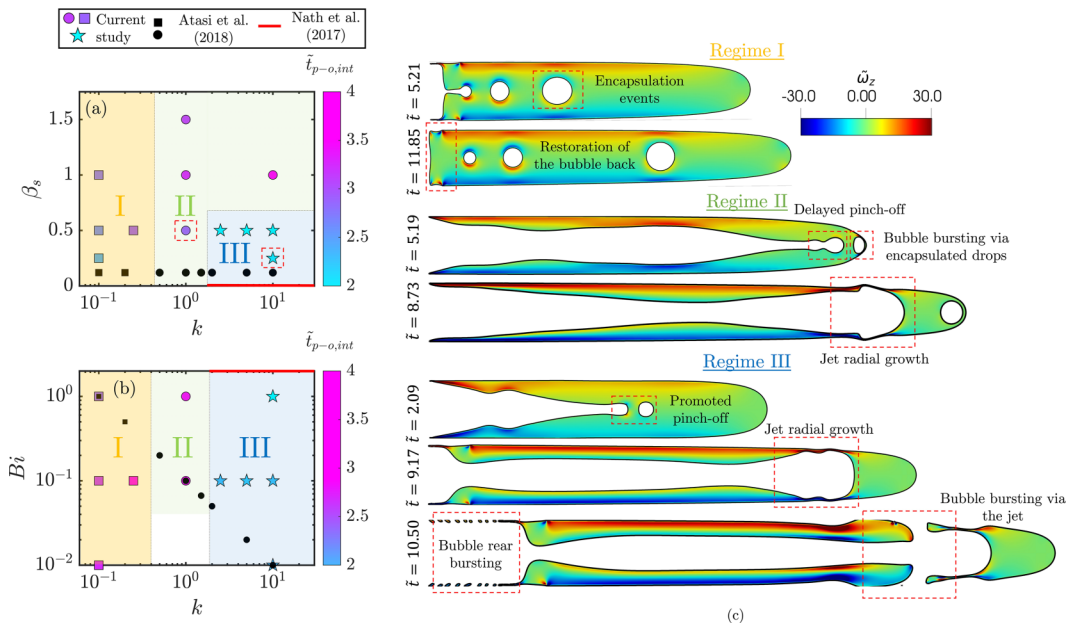


FIG. 11. Encapsulation and bursting regime maps in the (a) β_s - k and (b) Bi - k spaces. $Bi = 0.10$ for (a) and $\beta_s = 0.50$ for (b). Our results, shown as markers colored by the first interior pinch-off event, reveal three distinct regimes: I (squares), II (circles), and III (stars). The black markers correspond to the data set of Atasi *et al.* [39], which does not differentiate regime II from III. (c) Schematic contour plots of normalized vorticity in the z direction and comparison for the three regimes identified. All other parameters remain unchanged from those specified in Sec. II B for the base case. Regime maps developed for $Bo \rightarrow 0$.

The third regime (III) is confined to regions of above critical k with moderate β_s and $0.01 < Bi < 1$ and closely resembles the mechanisms of II, with the pinch-off times being the key differentiating characteristic. In III the fast expansion of the liquid jet expedites the first pinch-off with respect to the surfactant-free case (see previous subsection). Although the location of the first entrapment is much farther away from the bubble nose than in Sec. II, the encapsulated drops exhibit a comparatively faster velocity [e.g., $u_{x,d}/U_b = 1.27$ and $u_{x,d}/U_b = 1.47$ at $\tilde{t} = 4.75$ for the cases in Secs. II and III emphasized in Fig. 11(a), respectively], also leading to bubble nose ruptures by the drops and the consequent radial rupture by the bulbous end of the liquid jet mentioned above (see $\tilde{t} = 10.50$).

Figure 11 also displays the numerical data derived from the regime maps proposed in Atasi *et al.* [39] for surfactant-laden systems. A qualitative comparison is drawn between the bubble rear bursting phenomena characteristic of regime III [see $\tilde{t} = 10.50$ in Fig. 11(c)] and the observations of Nath *et al.* [37] for liquid-liquid flow in clean interfaces (see Fig. 15 of this reference). As depicted in the figure, our proposed transition from regime I (curvature inversion without bursting) to regimes II and III (bubble bursting) at $k \approx 0.45$ for varying β_s and Bi aligns remarkably well with that found in Atasi *et al.* [39] for $Ca \rightarrow 1$ (see Fig. 16 of this reference). Notice that Ref. [39] does not dive into the pinch-off dynamics of the system, precluding us from making a direct classification of their bubble bursting cases into our regimes II and III.

A few caveats are worth mentioning concerning these comparisons against previous investigations. While our regimes and observations of the bubble's behavior are entirely in line with previous results, we must emphasize that our operating conditions vary significantly from those of Atasi *et al.* [39] and Nath *et al.* [37]. The former reference explores a system with vanishing inertia, a close-to-spherical bubble, and a circular cross-sectional channel. The latter reference, as previously mentioned, involves the motion of a drop in the absence of surfactant material. These

characteristics explain why their encapsulation phenomena are observed for Ca much larger than ours [$Ca \sim O(10^0)$ compared to $Ca = 0.0693$] and why it is not possible to map the exact operating conditions of Nath *et al.* [37] into ours.

To finalize our analysis, we wish to highlight the limitations of our proposed encapsulation regime maps. As briefly mentioned in Sec. II A, gravitational forces are neglected in our simulations ($Bo = 0$) because their effects typically become significant only in channels larger than 1 mm [80], given the prevailing influence of capillary forces at the microscale. Our primary focus in this study was to characterize encapsulation mechanisms within scenarios involving inertia, noncircular geometries, and the presence of contaminants. Hence, isolating these influences from other nonidealities, including gravitational effects, was essential for our objectives. It is crucial to recognize, however, that the diminished influence of capillary forces—an essential condition for encapsulation, accentuated by surfactants—could potentially magnify the importance of gravitational forces, consequently impacting encapsulation dynamics.

We have assessed the potential impact of gravity by comparing characteristic timescales within our system to the free-falling time of an encapsulated drop. Adopting $Bo = 0.15$, a moderate value of Bo that still induces noticeable gravitational effects on gas-liquid systems [81]), we find that the falling time of encapsulated drops ($\approx 4.5 \times 10^{-2}$ s) largely exceeds the reentrant jet’s pinch-off times under our tested conditions ($\approx 5\text{--}7 \times 10^{-3}$ s) but is comparable to the total travel time of the bubble across our channel domain ($\approx 3\text{--}6 \times 10^{-2}$ s). This suggests that gravitational effects are unlikely to significantly influence the curvature inversion, jet infiltration, and breakup processes elucidated in this study, or the impact of surfactants. Nevertheless, gravity is certain to disrupt the trajectory, velocity of entrapped drops, and thus the proposed regime maps illustrated in Fig. 11.

IV. CONCLUDING REMARKS

This work presents an in-depth characterization of the unsteady mechanisms describing elongated bubbles flowing across liquid-filled channels via numerical simulations under negligible gravitational effects. These mechanisms arise in opposition to the well-known steady-state phenomena of Taylor bubbles under the traditional assumptions of negligible inertial/viscous effects, symmetric cross-sectional channels, and the absence of interfacial contaminants. As reported in limited instances (see Atasi *et al.* [39] and Sauzade and Cubaud [29]) and confirmed here, interesting dynamics emerge as $We \rightarrow O(10)$. Notably, the concomitant reduced capillary effects of high Ca (and We) induce a loss of sphericity at the bubble’s front and back, triggering an elongation in the flow direction of the former and a flattening and subsequent curvature inversion of the latter. The underlying mechanisms by which this curvature inversion evolves into a reentrant liquid jet infiltrating the bubble, how this liquid structure collapses into small liquid drops entrapped in the bubble domain, and the overall role of surfactants in these processes have been analyzed in detail. We emphasize the multiple parallels that can be readily drawn between the various interfacial features and singularities that ensue in our and other well-known systems involving capillary liquid breakup, such as inkjet printing, two-phase microfluidics, contracting liquid filaments, and sheet cavitation.

By performing a systematic sweep of a number of surfactant parameters and characterising dimensionless groups, we have elucidated the coupled effect of lower surface tension and Marangoni stresses and their interactions with inertia and viscosity. Two distinct modes of liquid jet breakup/drop encapsulation were found for comparatively low rates of surfactant adsorption (low k): one closure of the liquid jet at the bubble’s rear and one end-pinch breakup mode at the interior of the jet. Our simulations have shown that the combined and individual effects of both surface tension and Marangoni stresses induce a delayed response in terms of pinch-off times, as well as an inversion of the sequence of breakup modes with respect to clean interfaces. Provided that k is low enough, these effects are maintained for increasingly strong (large β_s) and less soluble (small Bi) surfactants. Under the baseline conditions considered, a critical value of $k = 1$ represents a phenomenological limit from which an increase of k represents an acceleration of the second mode

of jet breakup when compared to an uncontaminated interface. This is due to the fast and deep liquid infiltration in the bubble at high k , which promotes capillary breakup.

A summarizing map with three regimes of behavior was constructed in the β_s - k and Bi - k (Da) spaces, where regime I, limited by the critical k , allows for a semistable drop entrapment due to the eventual closure and restoration of the bubble back in the aftermath of pinch-off. Conversely, in regimes II (delayed pinch-off) and III (expedited pinch-off), the deep infiltration of the liquid jet that precedes end pinching, together with the high relative velocity of the entrapped drops are responsible for the subsequent bursting of the bubble nose. These two regimes, in addition, display a multitude of rich interfacial events following the liquid jet end pinching, including escapes from pinch-off, radial growth, and an eventual bubble bursting in the vicinity of the channel walls.

To the best of our knowledge, this is the first thorough and detailed characterization of the phenomenon of drop encapsulation in moving bubbles in the presence of surfactants. There are, however, a few avenues worthy of further pursuit in this topic, for instance, an examination of the influence of surfactant parameters, β_s , for example, on the critical k value. Based on our numerical results, it is likely that this critical k will decrease with increasing β_s , but additional evidence is required. A deeper exploration of the stability of the encapsulated drops in regime I may also be of interest to determine if there exists a set of conditions that allow for a perpetual entrapment of these drops, and the potential applications of such systems in the context of emulsification. Finally, an expansion of our proposed regime maps to include the effects of gravitational forces represents an interesting avenue for further research.

ACKNOWLEDGMENTS

This work is supported by the Engineering and Physical Sciences Research Council, United Kingdom, through the EPSRC MEMPHIS (EP/K003976/1) and PREMIERE (EP/T000414/1) Programme Grants, and by computing time at HPC facilities provided by the Research Computing Service. O.K.M. acknowledges funding from PETRONAS and the Royal Academy of Engineering for a Research Chair in Multiphase Fluid Dynamics. D.J. and J.C. acknowledge support through HPC/AI computing time at the Institut du Developpement et des Ressources en Informatique Scientifique (IDRIS) of the Centre National de la Recherche Scientifique (CNRS), coordinated by GENCI (Grand Equipement National de Calcul Intensif) Grant 2023 A0142B06721. P.P. acknowledges the doctoral scholarship from the Colombian Ministry of Science, Technology and Innovation, MINCIENCIAS. The authors acknowledge with gratitude A. Batchvarov for inspiring this work and for all fruitful discussions. We also acknowledge the helpful comments on the manuscript from A.D. Lavino.

The authors report no conflict of interest.

APPENDIX A: SURFACTANT PROPERTIES AND TIMESCALES

For typical ionic and nonionic surfactants in water, such as sodium dodecyl sulphate (SDS), N-dodecyl-N,N-dimethylammonio-3-propane sulfonate, and Triton X-100 (TX100), the value of Γ_∞ ranges between $O(10^{-6}$ to $10^{-5})$ mol/m² and D_s between $O(10^{-12}$ to $10^{-8})$ m²/s, which results in $\text{Pe}_s = O(10^3$ to $10^6)$ [77,82]. As noted previously in Constante-Amores *et al.* [83] and Batchvarov *et al.* [27], saturation of the system's dynamics is reached above $\text{Pe}_s \sim 100$. Pe_c was set to be equal to Pe_s , following the study of Agrawal and Neuman [84].

Based on Refs. [65,83] and our range of characterizing Oh, we define an inertial-capillary or Rayleigh timescale as $t_{\text{in-cap}} = \sqrt{\rho_l D^3 / \sigma_s}$, for $\text{Oh} \ll 1$ and a Marangoni timescale as $t_m = \sqrt{(\mu_l D) / \Delta\sigma}$, where $\Delta\sigma = \sigma_s - 0.05\sigma_s$ is a measurement of the surface tension gradients. The ranges for the characteristic timescales of the system are estimated to be $t_{\text{ad}} \sim O(10^{-4}$ to $10^0)$ s, $t_{\text{des}} \sim O(10^{-3}$ to $10^{-1})$ s, $t_{\text{in-cap}} \sim O(10^{-3}$ to $10^{-2})$ s, $t_{\text{conv}} \sim O(10^{-3}$ to $10^{-2})$ s, and $t_m \sim O(10^{-4})$ s (for surfactant-laden cases). These timescales ensure that sorptive/desorptive, inertial, capillary, and Marangoni phenomena will play an important role in the dynamics of the system.

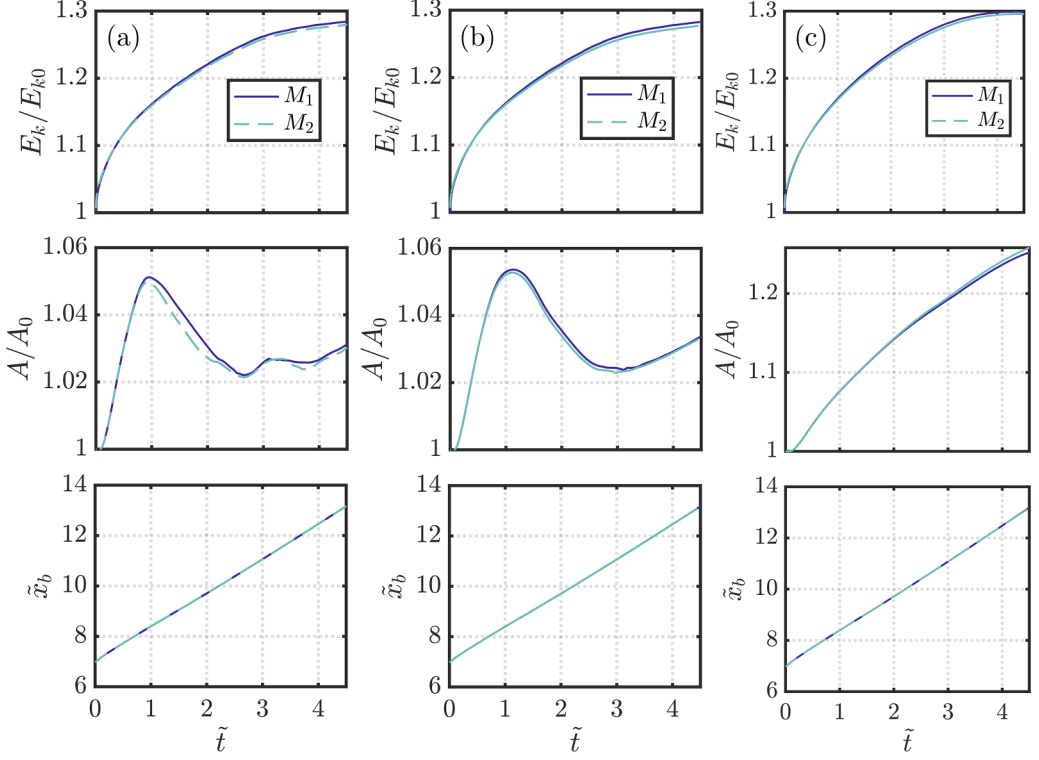


FIG. 12. Results of mesh independence study for surfactant-free and surfactant-laden cases. (a) Case 0 (surfactant-free); (b) Case 1; (c) Case 2.

APPENDIX B: MESH INDEPENDENCE AND RESOLUTION ANALYSIS

For the assessment of our results' (in)dependency on the mesh, we have tested two uniform Cartesian grids with varying resolutions on both surfactant-free and surfactant-laden cases. The operating conditions for all testing cases are those that allow the development of the liquid jet and drop encapsulation phenomenon, thus evaluating the resolution on small velocity and time scales.

Figure 12 depicts the temporal evolution of the kinetic energy, $E_k = \int_V (\rho \mathbf{u}^2)/2 dV$, the interfacial area, and the position of the bubble nose, \tilde{x}_b , the first two being normalized by their values at $\tilde{t} = 0$. The tested mesh resolutions correspond to $M_1 = 3456 \ 128 \ 128$ and $M_2 = 6912 \ 256 \ 256$, and the cases to surfactant-free for “Case 0” and surfactant-laden with $Da = 1$, $k = 0.1$ for “Case 1” and $Da = 0.1$, $k = 1$ for “Case 2.” All other parameters remain unchanged from those specified in Sec. II B. Table I reports a few additional features of the tested mesh resolutions, including the minimum cell size, Δx_{\min} , the maximum relative variation of the gas phase volume, $\Delta V_g = (V_g - V_{g0})/V_{g0}$, and that of the liquid phase, $\Delta V_l = (V_l - V_{l0})/V_{l0}$. Considering the adaptive nature of our time-step treatment (see Sec. II A), we highlight that modifying the mesh resolution alters the simulation time step in accordance to the cell size. For Case 1, we observed $\Delta t \approx 8 \times 10^{-7}$ s and $\Delta t \approx 4 \times 10^{-7}$ s for M_1 and M_2 , respectively. The almost complete overlapping of the plots displayed in Fig. 12 for the grids considered and the three sets of operating conditions suggests that increasing the resolution by twofold on each direction does not lead to the development of significantly different dynamics. Unless stated otherwise, all simulations have been run with M_1 given that it provides enough resolution to ensure mesh-independent results, while also requiring substantially less computational resources, as seen in Table I. This table also indicates that M_1

TABLE I. Additional features of the mesh resolutions tested.

Case name	Mesh	Computing time/CPU			
		to reach 10 ms (h)	Δx_{\min} (μm)	$\max(\Delta V_g)$ (%)	$\max(\Delta V_l)$ (%)
Case 0	M1	~ 0.60	7.81	7.70×10^{-3}	1.04×10^{-3}
	M2	~ 8.46	3.91	-6.13×10^{-3}	8.27×10^{-4}
Case 1	M1	~ 0.78	7.81	7.65×10^{-3}	3.02×10^{-4}
	M2	~ 12.71	3.91	3.84×10^{-3}	5.19×10^{-4}
Case 2	M1	~ 2.21	7.81	8.00×10^{-3}	2.61×10^{-4}
	M2	~ 7.34	3.91	7.28×10^{-3}	9.83×10^{-4}

allows us to achieve volume conservation for both phases with a deviation of 8×10^{-3} % or lower from the onset of the simulations.

An additional mesh independence test was carried out to specifically evaluate the pinch-off dynamics' sensitivity to the mesh resolution. For this test, we contrast the time taken to reach the curvature inversion, t_{inv} (described in Sec. III A), and the back and interior pinch-off times, $\tilde{t}_{p-o,bk}$ and $\tilde{t}_{p-o,int}$, respectively, for Case 0 and Case 1. Table II depicts these values for the two mesh resolutions considered. We note that both \tilde{t}_{p-o} are reported with \tilde{t}_{inv} as the reference frame. As a complement to the pinch-off times, we compare in Table III the size of the entrapped drops at selected times after the pinch-off event and before their stabilization [see Figs. 7(b) and 8(b)]. These results indicate that increasing the mesh resolution by a factor of 8 does not alter the dynamics at the locality of the pinch-off more than 3.5% for surfactant-free and surfactant-laden cases.

The mesh size selected also allowed to capture accurately the thin liquid film surrounding the bubble, which, according to previous works [18,85], requires a minimum of 5–10 computational cells covering its domain for a correct development of the liquid velocity profile. In our simulations, we have ensured the placement of at least five or six cells in the liquid film section for the cases that exhibit encapsulation ($We \sim 30$), for which $h(x)/D \sim 5^{-2}$ (see Fig. 11 of Magnini and Matar [18]). This condition is further achieved in the surfactant-laden simulations, which develop a thicker liquid film. We note, however, that the size of the entire domain, as well as the comprehensive sweep over dimensionless numbers presented, makes it prohibitively expensive in terms of computation to achieve the refinement levels reported in works such as Castrejón-Pita *et al.* [63] and Li and Sprittles [86] to fully capture all regime transitions leading to the interfacial singularities of pinch-off.

APPENDIX C: VALIDATION IN SQUARE CAPILLARIES

A supplementary validation for square capillary channels is conducted using the numerical data and conditions described in Magnini and Matar [18] for surfactant-free scenarios under non-negligible inertia. Satisfactory quantitative agreement between our results and those of Magnini and Matar [18] is achieved in terms of bubble-to-liquid velocity ratio, U_b/U_l , and gas area fraction, ϵ [see Figs. 13(a) and 13(b)], with maximum deviations of 2.7%; and 3.1%;, respectively. We

TABLE II. Recorded \tilde{t}_{inv} , $\tilde{t}_{p-o,bk}$, and $\tilde{t}_{p-o,int}$ for the two mesh resolutions tested. Values of $\Delta\tilde{t}$ represent the percent change of \tilde{t} going from M1 to M2.

	\tilde{t}_{inv}			$\tilde{t}_{p-o,bk}$			$\tilde{t}_{p-o,int}$		
	M1	M2	$\Delta\tilde{t}_{\text{inv}}$	M1	M2	$\Delta\tilde{t}_{p-o,bk}$	M1	M2	$\Delta\tilde{t}_{p-o,int}$
Case 0	0.122	0.120	-1.964%	2.158	2.098	-2.762%	2.328	2.265	-2.696%
Case 1	0.117	0.120	2.389%	2.904	2.829	-2.593%	2.647	2.563	-3.129%

TABLE III. Interfacial area (A_d in mm^2) of encapsulated drop after pinch-off. Values of ΔA_d represent the percent change of A_d going from M1 to M2.

	Case 0				Case 1			
\tilde{t}	2.979	3.422	3.865	4.308	2.984	3.427	3.870	4.313
A_d M1	0.800	0.762	0.755	0.754	0.713	0.709	0.709	0.709
A_d M2	0.777	0.747	0.739	0.741	0.693	0.693	0.697	0.694
ΔA_d	-2.943%	-1.898%	-2.242%	-1.714%	-2.805%	-2.257%	-1.693%	-2.116%

underline that the cases that do not have a direct counterpart from the above mentioned reference (i.e., $Ca = 0.0089$, $Ca = 0.0377$, and $Ca = 0.068$ for $Re = 443$) adequately follow the qualitative trend of increasing U_b/U_l and decreasing ϵ with Ca and Re .

Figures 13(c) and 13(d) exemplify the well-known bubble morphological regimes found in noncircular channels, as well as our model's correct capturing of the nonaxisymmetric bubble

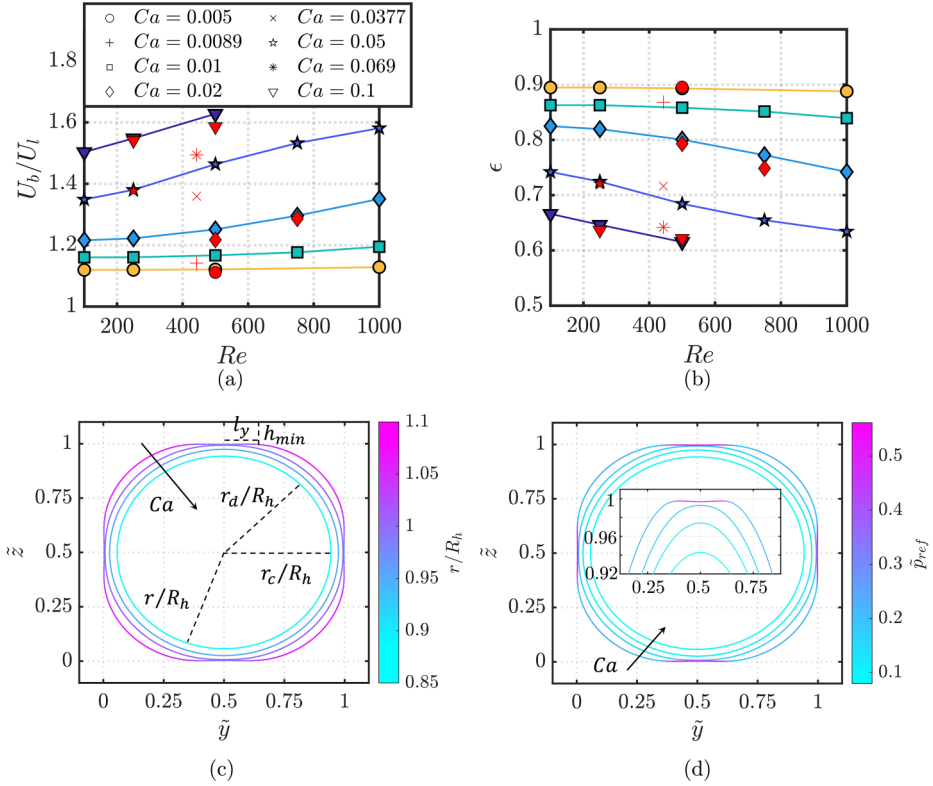


FIG. 13. Validation for square capillary channels and $We > 1$ in terms of (a) bubble nose velocity relative to average liquid phase velocity, and (b) gas phase area fraction. Each marker corresponds to a different Ca (as seen from the legend). Red represents our numerical results and the other colors the results of Magnini and Matar [18]. (c), (d) Replication of the bubble morphological structures proposed in the same reference with our numerical simulations in terms of (c) distance from channel center to any point of the interface normalized by the channel's hydraulic radius, R_h , and (d) normalized relative pressure, $\bar{p}_{ref} = (p - p_b)/\rho_l U_a^2$. From outermost to innermost series, we show our results for $Ca = 0.0089$, $Ca = 0.02$, $Ca = 0.0377$, and $Ca = 0.1$ at $Re = 443$ –500. Results in (b)–(d) are measured at a cross-sectional plane normal to the streamwise direction located at a distance of $5.5D$ behind the bubble nose, as reported in Magnini and Matar [18].

shapes that arise below a threshold Ca [16,87,88]. In accordance with Ferrari *et al.* [89], the corner flow effects exhibited in $Ca \lesssim 0.01$ promote the development of a saddle-shaped interface near the channel center lines [see outermost series in Figs. 13(c) and 13(d)], which brings about the formation of four lobes projecting towards the channel corners. As portrayed in Fig. 13(c), these lobes are located farthest from the channel center point (highest r/R_h) and will continue to grow as the saddle deepens ($r_d > r_c$) with decreasing Ca . The presence of the saddle shifts the minimum liquid film thickness, h_{\min} , from the center line of the channel to a position, l_y , that varies as a function of Ca . We compute $l_y/R_h = 0.2$ for the case highlighted in the figure, which matches remarkably well the value reported by Magnini and Matar [18] for $We \ll 1$ [$l_y/R_h \approx 0.195$; see Fig. 7(b) of the reference]. The high pressure zones at the saddles showcased in Fig. 13(d) are evidence of significant capillary flow drainage away from the thin-liquid film region, as reported in Magnini and Matar [18].

The other morphological regimes represented in Figs. 13(c) and 13(d) correspond to an additional nonaxisymmetric cross-sectional regime for $0.01 \lesssim Ca \lesssim 0.05$, characterized by $r_d > r_c$ and the absence of the saddle ($l_y = 0$; see $Ca = 0.02$ in the figure), and a fully symmetric bubble topology ($r_d = r_c$; see $Ca = 0.1$ in the figure) for the final regime. We draw attention to the almost perfect alignment of these regimes and the ranges of Ca in which they occur between our numerical predictions and those of the literature, notwithstanding that the regimes documented in the literature were observed under conditions of vanishing inertia.

-
- [1] A. Etminan, Y. S. Muzychka, and K. Pope, A review on the hydrodynamics of Taylor flow in microchannels: Experimental and computational studies, *Processes* **9**, 870 (2021).
 - [2] F. P. Bretherton, The motion of long bubbles in tubes, *J. Fluid Mech.* **10**, 166 (1961).
 - [3] G. I. Taylor, Deposition of a viscous fluid on a plane surface, *J. Fluid Mech.* **9**, 218 (1960).
 - [4] L. W. Schwartz, H. M. Princen, and A. D. Kiss, On the motion of bubbles in capillary tubes, *J. Fluid Mech.* **172**, 259 (1986).
 - [5] T. G. Karayiannis and M. M. Mahmoud, Flow boiling in microchannels: Fundamentals and applications, *Appl. Therm. Eng.* **115**, 1372 (2017).
 - [6] S. Shim, J. Wan, S. Hilgenfeldt, P. D. Panchal, and H. A. Stone, Dissolution without disappearing: Multicomponent gas exchange for CO₂ bubbles in a microfluidic channel, *Lab Chip* **14**, 2428 (2014).
 - [7] M. Heil, A. L. Hazel, and J. A. Smith, The mechanics of airway closure, *Respir. Physiol. Neurobiol.* **163**, 214 (2008).
 - [8] C. R. Carrigan and J. C. Eichelberger, Zoning of magmas by viscosity in volcanic conduits, *Nature (London)* **343**, 248 (1990).
 - [9] P. Aussillous and D. Quere, Quick deposition of a fluid on the wall of a tube, *Phys. Fluids* **12**, 2367 (2000).
 - [10] M. J. Martinez and K. S. Udell, Axisymmetric creeping motion of drops through circular tubes, *J. Fluid Mech.* **210**, 565 (1990).
 - [11] Y. Han and N. Shikazono, Measurement of the liquid film thickness in micro tube slug flow, *Int. J. Heat Fluid Flow* **30**, 842 (2009).
 - [12] H. Wong, C. J. Radke, and S. Morris, The motion of long bubbles in polygonal capillaries. Part 2. Drag, fluid pressure and fluid flow, *J. Fluid Mech.* **292**, 95 (1995).
 - [13] A. de Ryck, The effect of weak inertia on the emptying of a tube, *Phys. Fluids* **14**, 2102 (2002).
 - [14] S. Khodaparast, M. Magnini, N. Borhani, and J. R. Thome, Dynamics of isolated confined air bubbles in liquid flows through circular microchannels: An experimental and numerical study, *Microfluid. Nanofluid.* **19**, 209 (2015).
 - [15] M. D. Giavedoni and F. A. Saita, The rear meniscus of a long bubble steadily displacing a Newtonian liquid in a capillary tube, *Phys. Fluids* **11**, 786 (1999).
 - [16] H. Chen, Q. Meng, and J. Li, Thin lubrication film around moving bubbles measured in square microchannels, *Appl. Phys. Lett.* **107**, 141608 (2015).

- [17] H. Chen, Z. Li, and J. Li, Thin-film profile around long bubbles in square microchannels measured by chromatic interference method, *Appl. Phys. Lett.* **109**, 041604 (2016).
- [18] M. Magnini and O. K. Matar, Morphology of long gas bubbles propagating in square capillaries, *Int. J. Multiphase Flow* **129**, 103353 (2020).
- [19] M. Magnini, F. Mucicchi, I. El Mellas, and M. Icardi, Liquid film distribution around long gas bubbles propagating in rectangular capillaries, *Int. J. Multiphase Flow* **148**, 103939 (2022).
- [20] J. R. Lister, J. M. Rallison, A. A. King, L. J. Cummings, and O. E. Jensen, Capillary drainage of an annular film: The dynamics of collars and lobes, *J. Fluid Mech.* **552**, 311 (2006).
- [21] M. Sauzade and T. Cubaud, Bubble deformations and segmented flows in corrugated microchannels at large capillary numbers, *Phys. Rev. Fluids* **3**, 034202 (2018).
- [22] U. Olgac and M. Muradoglu, Effects of surfactant on liquid film thickness in the Bretherton problem, *Int. J. Multiphase Flow* **48**, 58 (2013).
- [23] S. N. Ghadiali and D. P. Gaver, The influence of non-equilibrium surfactant dynamics on the flow of a semi-infinite bubble in a rigid cylindrical capillary tube, *J. Fluid Mech.* **478**, 165 (2003).
- [24] G. M. Ginley and C. J. Radke, Influence of soluble surfactants on the flow of long bubbles through a cylindrical capillary, *ACS Symp. Ser.* **396**, 480 (1989).
- [25] Z. Y. Luo, X. L. Shang, and B. F. Bai, Effect of soluble surfactant on the motion of a confined droplet in a square microchannel, *Phys. Fluids* **31**, 117104 (2019).
- [26] A. Borhan and C. F. Mao, Effect of surfactants on the motion of drops through circular tubes, *Phys. Fluids A* **4**, 2628 (1992).
- [27] A. Batchvarov, L. Kahouadji, M. Magnini, C. R. Constante-Amores, S. Shin, J. Chergui, D. Juric, R. V. Craster, and O. K. Matar, Effect of surfactant on elongated bubbles in capillary tubes at high Reynolds number, *Phys. Rev. Fluids* **5**, 093605 (2020).
- [28] H. A. Abubakar and O. K. Matar, Linear stability analysis of Taylor bubble motion in downward flowing liquids in vertical tubes, *J. Fluid Mech.* **941**, A2 (2022).
- [29] M. Sauzade and T. Cubaud, Initial microfluidic dissolution regime of CO₂ bubbles in viscous oils, *Phys. Rev. E* **88**, 051001 (2013).
- [30] T. Taha and Z. F. Cui, CFD modelling of slug flow inside square capillaries, *Chem. Eng. Sci.* **61**, 665 (2006).
- [31] P. F. Pelz, T. Keil, and T. F. Groß, The transition from sheet to cloud cavitation, *J. Fluid Mech.* **817**, 439 (2017).
- [32] H. L. Goldsmith and S. G. Mason, The flow of suspensions through tubes. II. Single large bubbles, *J. Colloid Sci.* **18**, 237 (1963).
- [33] W. L. Olbricht and D. M. Kung, The deformation and breakup of liquid drops in low Reynolds number flow through a capillary, *Phys. Fluids A* **4**, 1347 (1992).
- [34] T. M. Tsai and M. J. Miksis, Dynamics of a drop in a constricted capillary tube, *J. Fluid Mech.* **274**, 197 (1994).
- [35] D. Izbassarov and M. Muradoglu, A computational study of two-phase viscoelastic systems in a capillary tube with a sudden contraction/expansion, *Phys. Fluids* **28**, 012110 (2016).
- [36] C. Pozrikidis, The buoyancy-driven motion of a train of viscous drops within a cylindrical tube, *J. Fluid Mech.* **237**, 627 (1992).
- [37] B. Nath, G. Biswas, A. Dalal, and K. C. Sahu, Migration of a droplet in a cylindrical tube in the creeping flow regime, *Phys. Rev. E* **95**, 033110 (2017).
- [38] M. Andreadaki, A. Georgoulas, N. Miché, and M. Marengo, Accelerating Taylor bubbles within circular capillary channels: Break-up mechanisms and regimes, *Int. J. Multiphase Flow* **134**, 103488 (2021).
- [39] O. Atasi, B. Haut, A. Pedrono, B. Scheid, and D. Legendre, Influence of soluble surfactants and deformation on the dynamics of centered bubbles in cylindrical microchannels, *Langmuir* **34**, 10048 (2018).
- [40] A. Martínez-Calvo, J. Rivero-Rodríguez, B. Scheid, and A. Sevilla, Natural break-up and satellite formation regimes of surfactant-laden liquid threads, *J. Fluid Mech.* **883**, A35 (2020).
- [41] S. Shin and D. Juric, Modeling three-dimensional multiphase flow using a level contour reconstruction method for front tracking without connectivity, *J. Comput. Phys.* **180**, 427 (2002).

- [42] S. Shin, J. Chergui, D. Juric, L. Kahouadji, O. K. Matar, and R. V. Craster, A hybrid interface tracking-level set technique for multiphase flow with soluble surfactant, *J. Comput. Phys.* **359**, 409 (2018).
- [43] S. Shin and D. Juric, A hybrid interface method for three-dimensional multiphase flows based on front tracking and level set techniques, *Int. J. Numer. Methods Fluids* **60**, 753 (2009).
- [44] S. Shin, J. Chergui, and D. Juric, A solver for massively parallel direct numerical simulation of three-dimensional multiphase flows, *J. Mech. Sci. Technol.* **31**, 1739 (2017).
- [45] M. Muradoglu and G. Tryggvason, Simulations of soluble surfactants in 3D multiphase flow, *J. Comput. Phys.* **274**, 737 (2014).
- [46] C. W. Shu and S. Osher, Efficient implementation of essentially non-oscillatory shock-capturing schemes, II, *J. Comput. Phys.* **83**, 32 (1989).
- [47] M. Sussman, E. Fatemi, P. Smereka, and S. Osher, An improved level set method for incompressible two-phase flows, *Comput. Fluids* **27**, 663 (1998).
- [48] Y. X. Wang and J. M. Wen, Gear method for solving differential equations of gear systems, *J. Phys.: Conf. Ser.* **48**, 143 (2006).
- [49] C. R. Constante-Amores, L. Kahouadji, A. Batchvarov, S. Shin, J. Chergui, D. Juric, and O. K. Matar, Dynamics of retracting surfactant-laden ligaments at intermediate Ohnesorge number, *Phys. Rev. Fluids* **5**, 084007 (2020).
- [50] C. R. Constante-Amores, L. Kahouadji, A. Batchvarov, S. Shin, J. Chergui, D. Juric, and O. K. Matar, Direct numerical simulations of transient turbulent jets: Vortex-interface interactions, *J. Fluid Mech.* **922**, A6 (2021).
- [51] R. K. Edvinsson and S. Irandoust, Finite-element analysis of Taylor flow, *AIChE J.* **42**, 1815 (1996).
- [52] M. Magnini, A. Ferrari, J. R. Thome, and H. A. Stone, Undulations on the surface of elongated bubbles in confined gas-liquid flows, *Phys. Rev. Fluids* **2**, 084001 (2017).
- [53] A. A. Castrejón-Pita, J. R. Castrejón-Pita, and I. M. Hutchings, Breakup of liquid filaments, *Phys. Rev. Lett.* **108**, 074506 (2012).
- [54] J. Eggers and E. Villermaux, Physics of liquid jets, *Rep. Prog. Phys.* **71**, 036601 (2008).
- [55] B. Ambravaneswaran, H. J. Subramani, S. D. Phillips, and O. A. Basaran, Dripping-jetting transitions in a dripping faucet, *Phys. Rev. Lett.* **93**, 034501 (2004).
- [56] T. Driessen, R. Jeurissen, H. Wijnshoff, F. Toschi, and D. Lohse, Stability of viscous long liquid filaments, *Phys. Fluids* **25**, 062109 (2013).
- [57] P. K. Notz and O. A. Basaran, Dynamics and breakup of a contracting liquid filament, *J. Fluid Mech.* **512**, 1 (2004).
- [58] J. Hoepffner and G. Paré, Recoil of a liquid filament: Escape from pinch-off through creation of a vortex ring, *J. Fluid Mech.* **734**, 183 (2013).
- [59] F. Wang, F. P. Contò, N. Naz, J. R. Castrejón-Pita, A. A. Castrejón-Pita, C. G. Bailey, W. Wang, J. J. Feng, and Y. Sui, A fate-alternating transitional regime in contracting liquid filaments, *J. Fluid Mech.* **860**, 640 (2019).
- [60] J. Eggers, J. R. Lister, and H. A. Stone, Coalescence of liquid drops, *J. Fluid Mech.* **401**, 293 (1999).
- [61] J. Eggers, Universal pinching of 3D axisymmetric free-surface flow, *Phys. Rev. Lett.* **71**, 3458 (1993).
- [62] R. F. Day, E. J. Hinch, and J. R. Lister, Self-similar capillary pinchoff of an inviscid fluid, *Phys. Rev. Lett.* **80**, 704 (1998).
- [63] J. R. Castrejón-Pita, A. A. Castrejón-Pita, S. S. Thete, K. Sambath, I. M. Hutchings, J. Hinch, J. R. Lister, and O. A. Basaran, Plethora of transitions during breakup of liquid filaments, *Proc. Natl. Acad. Sci. USA* **112**, 4582 (2015).
- [64] R. V. Craster, O. K. Matar, and D. T. Papageorgiou, Pinchoff and satellite formation in compound viscous threads, *Phys. Fluids* **15**, 3409 (2003).
- [65] P. M. Kamat, B. W. Wagoner, S. S. Thete, and O. A. Basaran, Role of Marangoni stress during breakup of surfactant-covered liquid threads: Reduced rates of thinning and microthread cascades, *Phys. Rev. Fluids* **3**, 043602 (2018).
- [66] Y. C. Liao, E. I. Franses, and O. A. Basaran, Deformation and breakup of a stretching liquid bridge covered with an insoluble surfactant monolayer, *Phys. Fluids* **18**, 022101 (2006).

- [67] H. Wee, B. W. Wagoner, V. Garg, P. M. Kamat, and O. A. Basaran, Pinch-off of a surfactant-covered jet, *J. Fluid Mech.* **908**, A38 (2021)
- [68] Q. Xu, Y. C. Liao, and O. A. Basaran, Can surfactant be present at pinch-off of a liquid filament? *Phys. Rev. Lett.* **98**, 054503 (2007).
- [69] P. M. Kamat, B. W. Wagoner, A. A. Castrejón-Pita, J. R. Castrejón-Pita, C. R. Anthony, and O. A. Basaran, Surfactant-driven escape from endpinching during contraction of nearly inviscid filaments, *J. Fluid Mech.* **899**, A28 (2020).
- [70] E. Antonopoulou, O. G. Harlen, M. Rump, T. Segers, and M. A. Walkley, Effect of surfactants on jet break-up in drop-on-demand inkjet printing, *Phys. Fluids* **33**, 072112 (2021).
- [71] Y. Zhong, H. Fang, Q. Ma, and X. Dong, Analysis of droplet stability after ejection from an inkjet nozzle, *J. Fluid Mech.* **845**, 378 (2018).
- [72] B. Ambravaneswaran and O. A. Basaran, Effects of insoluble surfactants on the nonlinear deformation and breakup of stretching liquid bridges, *Phys. Fluids* **11**, 997 (1999).
- [73] S. Wang, Y. Zhong, and H. Fang, Deformation characteristics of a single droplet driven by a piezoelectric nozzle of the drop-on-demand inkjet system, *J. Fluid Mech.* **869**, 634 (2019).
- [74] L. Rayleigh, On the capillary phenomena of jets, *Proc. R. Soc. A* **29**, 71 (1879).
- [75] M. Kalli, P. Pico, L. Chagot, L. Kahouadji, S. Shin, J. Chergui, D. Juric, O. K. Matar, and P. Angeli, Effect of surfactants during drop formation in a microfluidic channel: A combined experimental and computational fluid dynamics approach, *J. Fluid Mech.* **961**, A15 (2023).
- [76] J. M. J. M. Gordillo and J. Rodríguez-Rodríguez, Capillary waves control the ejection of bubble bursting jets, *J. Fluid Mech.* **867**, 556 (2019).
- [77] C. R. Constante-Amores, L. Kahouadji, A. Batchvarov, S. Shin, J. Chergui, D. Juric, and O. K. Matar, Dynamics of a surfactant-laden bubble bursting through an interface, *J. Fluid Mech.* **911**, A57 (2021).
- [78] I. B. Bazhlekov, P. D. Anderson, and H. E. H. Meijer, Numerical investigation of the effect of insoluble surfactants on drop deformation and breakup in simple shear flow, *J. Colloid Interface Sci.* **298**, 369 (2006).
- [79] C. R. Anthony, P. M. Kamat, M. T. Harris, and O. A. Basaran, Dynamics of contracting filaments, *Phys. Rev. Fluids* **4**, 093601 (2019).
- [80] M. Magnini, S. Khodaparast, O. K. Matar, H. A. Stone, and J. R. Thome, Dynamics of long gas bubbles rising in a vertical tube in a cocurrent liquid flow, *Phys. Rev. Fluids* **4**, 023601 (2019).
- [81] H. R. Moran, M. Magnini, C. N. Markides, and O. K. Matar, Inertial and buoyancy effects on the flow of elongated bubbles in horizontal channels, *Int. J. Multiphase Flow* **135**, 103468 (2021).
- [82] M. Kalli, L. Chagot, and P. Angeli, Comparison of surfactant mass transfer with drop formation times from dynamic interfacial tension measurements in microchannels, *J. Colloid Interface Sci.* **605**, 204 (2022).
- [83] C. R. Constante-Amores, A. Batchvarov, L. Kahouadji, S. Shin, J. Chergui, D. Juric, and O. K. Matar, Role of surfactant-induced Marangoni stresses in drop-interface coalescence, *J. Fluid Mech.* **925**, A15 (2021).
- [84] M. L. Agrawal and R. D. Neuman, Surface diffusion in monomolecular films, *J. Colloid Interface Sci.* **121**, 366 (1988).
- [85] R. Gupta, D. F. Fletcher, and B. S. Haynes, On the CFD modelling of Taylor flow in microchannels, *Chem. Eng. Sci.* **64**, 2941 (2009).
- [86] Y. Li and J. E. Sprittles, Capillary breakup of a liquid bridge: Identifying regimes and transitions, *J. Fluid Mech.* **797**, 29 (2016).
- [87] A. L. Hazel and M. Heil, The steady propagation of a semi-infinite bubble into a tube of elliptical or rectangular cross-section, *J. Fluid Mech.* **470**, 91 (2002).
- [88] W. B. Kolb and R. L. Cerro, Coating the inside of a capillary of square cross section, *Chem. Eng. Sci.* **46**, 2181 (1991).
- [89] A. Ferrari, M. Magnini, and J. R. Thome, Numerical analysis of slug flow boiling in square microchannels, *Int. J. Heat Mass Transf.* **123**, 928 (2018).